THESIS FOR THE DEGREE OF LICENTIATE OF PHILOSOPHY

ASPECTS ON MEASURING ELECTRICAL CURRENT UTILIZING MAGNETIC ZERO-FLUX TECHNIQUE

MARIA HAMMARQVIST

High Voltage Engineering
Department of Materials and Manufacturing Technology
CHALMERS UNIVERSITY OF TECHNOLOGY
Göteborg, Sweden, 2018

ASPECTS ON MEASURING ELECTRICAL CURRENT UTILIZING MAGNETIC ZERO-FLUX TECHNIQUE

MARIA HAMMARQVIST

Göteborg, April 2018

Licentiatsavhandlingar vid Chalmers tekniska högskola
Ny serie
ISSN 1403-266X R003/2018

Technical report
ISSN 1403-266X R003/2018

High Voltage Engineering
Department of Electrical Engineering
Chalmers University of Technology, SE-412 96 Göteborg, Sweden
Phone: +46 (0) 31 772 1000

Printed by Bibliotekets reproservice, Chalmers University of Technology
Göteborg, Sweden, April 2018

Abstract

The utilization of high accuracy measurements of electrical quantities is a prerequisite for the development of modern society. Generally, measurements serve different purposes and hence the criteria for the measurement equipment and method are different. For example, the demands are mild if the application is the continuous monitoring of the power grid, more finely tuned for measuring methods used in research and development, and often challenging in the case of certified measuring methods adequate for calibration and accreditation. RISE Research Institutes of Sweden (former SP Technical Research Institute of Sweden) is appointed the National Metrology Institute by the Swedish government for electrical quantities and continuously develops and provides measurement technology for the different needs governed by application.

The magnetic zero-flux technique is a non-contact measurement method for electrical AC and DC current and its design principle enables accurate measurements over a large current range. Its advantages come however with the price of a complex but sophisticated design. The zero-flux technique has been utilized for many decades, and there are a number of manufacturers providing commercial systems with somewhat different features.

This project is devoted to the further investigation and advancement of some metrological aspects of the magnetic zero-flux technique for AC. Practical laboratory tests on a state-of-the-art zero-flux system are used to create a picture of its properties at higher frequencies than its manufacturer has provided detailed specifications for. Focus is to determine how sensitive the measurement results are to practical arrangements and limitations of the measurement setup. A method and guide to how different configurations of the measurement setup affect the measured results in different frequency ranges is provided. Utilizing this characterization, practical set-ups can be made, as optimal as possible for the frequency range of interest, avoiding time-consuming focus on aspects not relevant for the specific application.

The identified aspects of interest are: (i) identifying the source of the measurement error in the zero-flux system's design and, if possible, minimizing this error by design adjustments, (ii) measurement error and measurement uncertainty of a zero-flux system in presence of geometric asymmetry and disturbance from return or nearby conductors, (iii) simultaneous measurements of sinusoidal signals of different amplitudes, frequencies and phase angles, (iiii) detection of sub-synchronous events, and (v) non-steady state phenomena, like for example transients in the drive line of electrical vehicles. In this thesis, aspects (i) and (ii) above are in focus. Some conclusions can be drawn based on the performed study concerning aspect (iiii), whereas aspects (iii) and (v) remain out of its scope.

The initial step of this project was the choice of a generally applicable method for characterization and evaluation of a zero-flux system. The method chosen is the combination of a coaxial primary current path, or as near coaxial as was practically convenient, and a Digital Sampling Watt Meter (DSWM). The method can be utilized for the characterization and evaluation of other zero-flux systems. An investigation was performed to decide from which part of the construction the phase angle error stems. The performed characterization allowed compensating for the errors, making the measurement accuracy greatly improved. Two modifications to the circuitry of the zero-flux systems were introduced and evaluated, both of which yielded improvement of its high frequency characteristics up to 100 kHz. Also the accuracy within the low frequency range (from 10 – 50 Hz) was improved by one of the modifications.

The error of a zero-flux measuring system depends on the positioning of its sensor around the conductor carrying the measured current and the geometry of the primary current path. The total error increases with frequency, but which geometric factor that is the most important one varies with frequency. In this study, utilizing sinusoidal primary current, it was found that for 50 Hz, tilt of the sensor and positioning of the connection point for the measurement and zero-flux control cable (rotation) caused the largest effects on the scale factor. De-centring and the distances to different parts of the return conductor were less important in the 50 Hz case. For 25 kHz, de-centring and rotation were the main contributors to scale factor change, while tilt had the smallest measured effect. The total contribution from sensor positioning in the magnetic field to the expanded measurement uncertainty was estimated to 0.0024 % in the 50 Hz case, to 0.0040 % for 1 kHz, to 0.14 % for 10 kHz, and to 0.41 % for 25 kHz.

Keywords: *AC Current, Current Transformer, Frequency Response, Zero-Flux Measurement Technique, Measurement Uncertainty, Traceability, Zero-Flux*

To Magnus and Fredrik

Acknowledgement

This licentiate project was performed as an Industrial PhD project between Chalmers University of Technology and SP Technical Research Institute of Sweden (now RISE Research Institutes of Sweden, from now on referred to as RISE) and was financed by Chalmers Energy Initiative, (CEI) and by Wise Measurements for Smart Grids (WMSG). CEI was one of Chalmers' eight Areas of Advance, based on funding for strategically important research areas by the Swedish government. CEI was followed by one of Chalmers' Areas of Advance, "Energy". WMSG is a competence platform at RISE.
The author wishes to thank Prof. Stanislaw Gubanski, Chalmers University of Technology, and Anders Mannikoff, CEO at Herrljunga Elektriska, for initializing this project and their valuable contributions in different stages of the project, Assoc. Prof. Jörgen Blennow at Chalmers University of Technology, Alf-Peter Elg and Anders Bergman at RISE for their supervision, Jan Wolbert and Ramon Lachminarainsingh (CEO) at PM Special Measuring Systems B.V. for providing equipment and for valuable discussions, and all colleagues at RISE and Chalmers. First and last, thanks to my family and especially to my sons Magnus and Fredrik.

Borås
April 2018 *Maria Hammarqvist*

Abbreviations and definitions in the text

φ_{DUT}	Phase angle for the zero-flux system
φ_{ref}	Phase angle for the reference DSWM shunt. φ_{ref} is set to zero in this work.
$\Delta\varphi$	Phase angle error (or phase error) of the zero-flux system. The unit is radians. Calculated as $\Delta\varphi = \varphi_{DUT} - \varphi_{ref}$, or in words; the phase difference between the zero-flux system (DUT) and the reference shunt.
$\Delta\varphi/f$	Phase angle error divided by frequency. The unit is seconds
I_{prim}	Current (in Ampere) through the primary circuit
R_{shunt}	Resistance of the reference DSWM shunt
V_{DUT}	Output voltage from the zero-flux system under test
V_{output}	Same as above, the two used alternately
V_{ref}	Voltage over the reference DSWM shunt
BIPM	Bureau International des Poids et Mesures. Organization for the national metrology institutes, situated in Paris. Among other things responsible for the internationally recognized CMC tables (see next entry).
CMC	Calibration and Measurement Capability, the lowest achievable traceable measurement uncertainty values that an NMI (see below) may issue. Reported to and approved by the BIPM.
Combined standard uncertainty	Denoted u. Calculated as the root-summed-square (the square root of the sum of the contributions squared) of the standard uncertainties.
DMM	Digital Multimeter
DVM	Digital Volt Meter
DSWM	Digital Sampling Watt Meter. A two channel measuring system utilizing synchronized digital sampling to achieve low measurement uncertainty for AC signals. Measures one voltage and one current, two voltages or two currents.
DUT	Device Under Test, or the test object
EA 4/02	Full name: "EA-4/02 Expression of the Uncertainty of Measurement in Calibration (previously EAL-R2)". A slightly simplified standard procedure for the calculation of measurement uncertainty. Guide issued by the European co-operation for Accreditation, EA, following GUM (see below).
Expanded (measurement) uncertainty	Denoted U. In this work calculated as 2 times the combined standard uncertainty. Other factors than 2 may be used.
GUM	Guide to the Expression of Uncertainty in Measurement. Full name: "ISO/IEC Guide 98-3:2008 Uncertainty of measurement -- Part 3: Guide to the expression of uncertainty in measurement (GUM:1995)". Gives general rules for the evaluation of and correct expression of uncertainty in measurement. Generally recognized and adhered to by the NMI society.
ISO/IEC 17025	"ISO/IEC 17025:2005 General requirements for the competence of testing and calibration laboratories" Standard followed by accredited laboratories and NMI's .
L	Inductance

NMI	National Metrology Institute, a measurement institute appointed by the state to - among other things - serve industry with quality assured measurements.
ppm	Parts per million, when utilized in the text, the value is also given in percent. No longer a correct term according to standards, but still sometimes practical.
PXI	PCI eXtensions for Instrumentation. National Instruments' PC-based modular platform for measurement and automation systems.
SF	Scale factor. When calibrating a measuring system, the *SF* can be one of the resulting parameters. True value of the measuring system is equal to the *SF* times the system output. In this text defined as I_{prim}/V_{output}, or in words; the primary current through the sensor of the zero-flux system divided by its output voltage.
Standard uncertainty	Uncertainty of the result of a measurement expressed as a standard deviation.
Swedac	Swedish Board of Accreditation and Conformity Assessment. Supervises accredited laboratories.
StAcc	Manufacturers model name for "standard accuracy"
TopAcc	Manufacturers model name for "top accuracy", referring to DC

Table of contents

1 Introduction

1.1 Some words about measurements

THIS section gives some basic concepts from the vast field of traceable metrology which is where National Metrology Institutes (NMI), like RISE, have their bases. The purpose is to give some background to why research related mainly to measurements, as in this work, is performed. It also serves to facilitate the understanding of discussions and reasoning throughout the thesis and provide some general background for the aim of the project. The interested reader can find a popular background to metrology (the science of measurements) in for example [1], or a more complete background in for example [2].

Correct measurements are a prerequisite for trade, both internationally and locally. Without the trust based on that buyer and seller agree on what quantity is payed for, basic human interactions on which society rests would be impossible. To ensure maximum correctness and maximum trust, a worldwide system for metrology has been developed during the decades.

The corner stone in this worldwide system is the Bureau International des Poids et Mesures, BIPM, which with its roots in the metre convention, was established by international treaty in 1875 and still forms the basis for international agreements concerning metrology. BIPM coordinates research and agreements concerning the SI-system and the realizations of the units (in simple words; how they are brought from theory to practical use). The SI system defines the units (kilogram, meter, second, ampere, kelvin, mole and candela) and states how these are realized. The purpose of this cooperation is that the same value of the units can be realized anywhere in the world.

The realizations involve complicated and costly scientific work and are often, but not necessarily, performed by NMIs. NMIs are appointed by governments and given the role of providing measurements and calibrations traceable to the realizations to industry and society, which is relevant both for production and research. The realizations are costly, not the least concerning the competence that has to be built up, so NMIs generally choose and prioritize when and in which order to obtain in-house traceability. The Swedish NMI, RISE Research Institutes of Sweden (RISE), has in-house traceability for all electrical SI-units, and continuously develops the traceability in the case of AC. Traceability for AC is a never-ending story, as the realizations can always be extended to new frequency ranges.

To ensure that the realizations actually end up with compatible results worldwide, international inter-comparisons are performed; an artefact (an object of highest possible stability) is passed around to and measured by the different NMIs. The true value of the artefact is then calculated from all the reported results which are given different weights according to the quality of the results as defined in a decided procedure. The procedure to complete one international inter-comparison can take several years, since uttermost care must be taken by the participants concerning measurements, calculations and transportation of the artefact.

Below the level of NMIs, there are accredited laboratories, supervised by national accreditation boards, like for example Swedac in Sweden. In the case of traceable measurements, IEC/ISO 17025 and IEC/ISO 17020 are the relevant standards. Accredited laboratories generally buy their traceability from an NMI, both via calibration (establishing an instrument's or standard's deviation from the true value) and inter-comparisons. An inter-comparison for accredited laboratories is different from the international inter-comparisons between NMIs regarding how the true value of the artefact is calculated. The value in an inter-comparison for accredited laboratories is simply set by the NMI providing the artefact, and not calculated from the values of all the participants, as is the case for an international inter-comparison between NMIs.

Within metrology, the goal is to measure and observe without disturbing the process to be analysed. Further, all kinds of irregularities within the collected data need to be found and addressed. For the metrology world in general and for the NMIs especially, whose mission is to serve the market with high-quality and traceable calibration and measurement services, the main challenge is to ensure that their measurements are indisputable even when faced with external interference or distortions. For the

author, as being involved in measurements related to transmission and distribution of electrical energy, this has a special flavour in that modern electrical equipment in diverse functions, from the high power grid to the consumer market, give rise to more distortion than has historically been the case. Simultaneously, deregulations make correct measurements more demanded and important than ever.

There is a need to scrutinize traditional measurement methods, ascertain their effects and roles in today´s and tomorrow´s electrical systems and determine the boundaries for traditional methods. More specifically, there is a need to quantify measurement errors when measurement methods are applied outside their prevalent area of use, and invent and further develop measurement methods for the identification and quantification of, for example, transients and superimposed signals which have earlier been insignificant in traditional applications, but which can prove important in modern applications. One first step could be to raise a warning flag, but a more proactive role is to be on the frontline and develop modifications of existing measurement methods, as well as develop new metrology methods fit for the new challenges that society meets. New technical solutions emerge, and large resources are spent on their development. The NMIs in particular must be prepared to assist in this process with knowledge and measurement resources. The task is gigantic, but also a challenge and an obligation to undertake.

This task can be addressed in different ways; one strategy could be to make a general plan for needed contributions, and based on this plan build a separate organisation. Another, more efficient, strategy is to proceed with development in areas already known – with measurement instruments available on the market, with already developed measurement methods et cetera – and advance knowledge, area by area. The nature of the investigations presented in this work is of this latter type. Hopefully it can serve as inspiration for others to "dig where you stand" considering today's and tomorrow's demands. As often, some practical knowledge is better than gigantic visions demanding large resources.

No matter what type of measurement that is performed, the measurement result always has two inseparable parts, the measured *value* itself and its associated measurement *uncertainty*. These two parts will now be briefly discussed. The measured value will always be somewhat different from the "true" value of the measured object, i.e. it has an error, due to imperfections in the measuring instrument, the measurement method, the operator performing the measurements, the ambient conditions etcetera. All these errors must be accounted for; some errors are known or predictable and can be corrected for by the known amount, directly affecting the measured value. Other errors cannot be reliably estimated and is therefore regarded as an uncertainty, i.e. a *parameter, associated with the result of a measurement that characterizes the dispersion of the values that could reasonably be attributed to the measurand*. There are standardized methods to calculate and express the measurement uncertainty, given in [3].

Traceability to the physical definitions of the quantities of interest, in our case volt, ohm, ampere, and second, is a key term, both to obtain a correct measurement value, and for the calculation of the measurement uncertainty. In simple terms, traceability means that the measurement error and the measurement uncertainty are known and accounted for in each and every one of the steps from the realization of the basic quantities to the measurement of interest. This is known as a traceability chain, and traceability charts are used to visualize the different methods and steps needed for a certain quantity. In Figure 1, RISE's traceability chart for AC power and energy is given. Note the Digital Sampling Watt Meter (DSWM), central in the figure, which is the reference system utilized in this investigation.

The vertical bars in the figure ("Phase error determination", "Resistance" and "AC voltage" have their own traceability charts behind them. For example, the definition of resistance follows from the quantum Hall effect and the fundamental constant known as the von Klitzing constant, R_k; AC voltage follows from the Josephson Effect and resistance and voltage are thereby defined only from fundamental constants. Note also the grey box labelled "International comparison", which is a corner stone in international measurement related co-operation and mutual acceptance between independent actors of each other's methods and results.

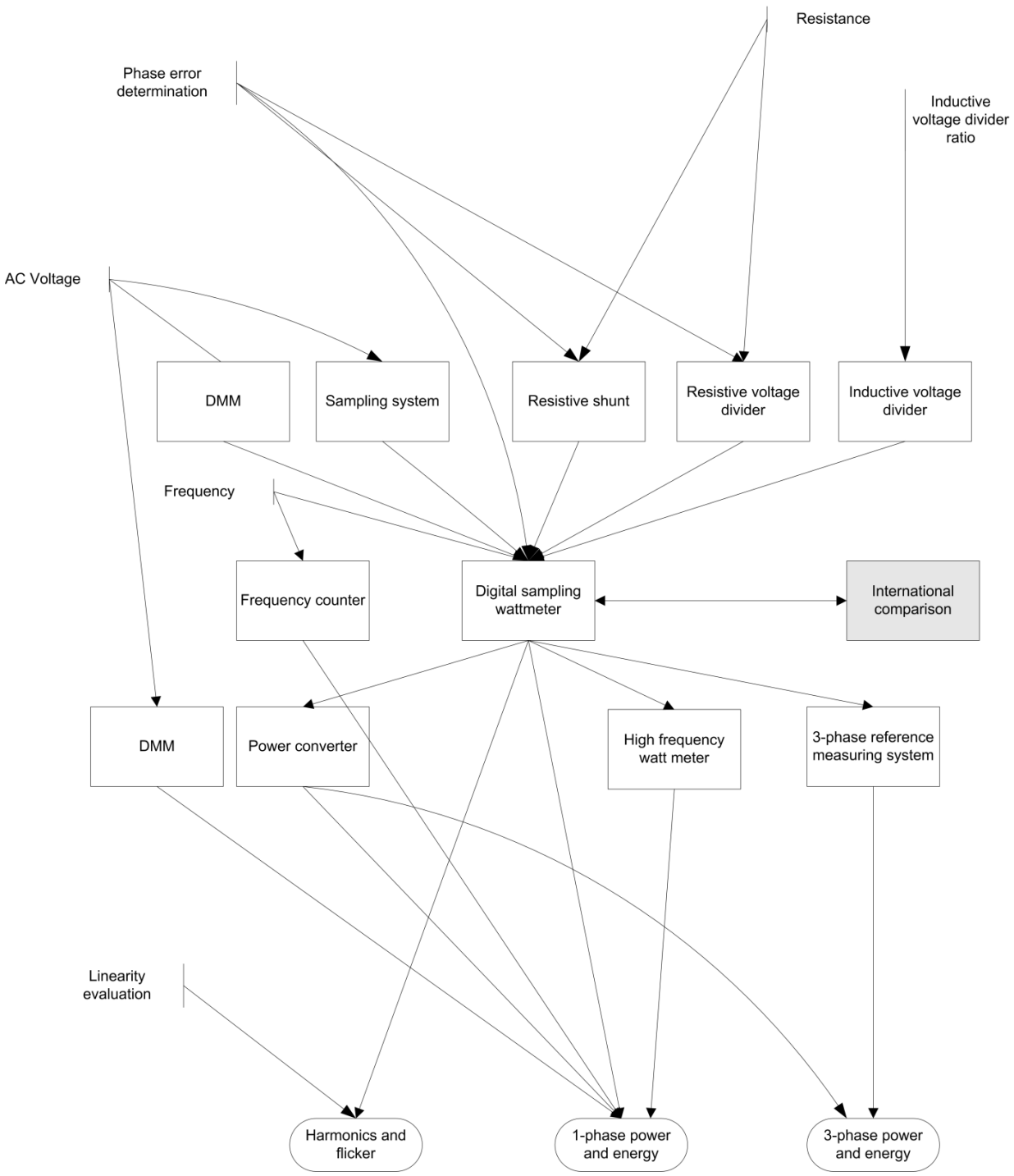

Figure 1: Example of a traceability chart, here for AC current, a measurand of interest in this thesis. The figure illustrates that in order to measure the three quantities at the bottom, calibrated equipment from the above square boxes are needed, as well as results from the realizations (marked by vertical bars). Note the digital sampling wattmeter in the centre of the figure, an equipment utilized in versatile measurements, including this work, and with a profound scientific effort behind it.

1.2 Research focus

THE utilization of high accuracy measurements of electrical quantities is a prerequisite for the development of modern society. In this respect, measurement of electrical currents by means of non-contact methods is utilized to avoid errors brought up by heating of the measuring devices as well as when interruptions for installation or repair of galvanically connected measurement equipment in electrical circuits are undesired. The magnetic zero-flux technique, earliest found reports in [4] and [5], stemming from the traditional measurement by current transformer, is such a non-contact measurement method and relies on minimizing flux in the core of the measuring sensor. Its design principle provides advantages from a metrological point of view due to inherent attributes, such as a low range-dependence (error minimization is a natural consequence of the reduction of magnetization in the transformer core [6]), and a possibility to measure currents ranging from DC, via AC currents of low frequencies, to AC currents of several kHz. The ability to measure both DC and AC comes however with the price of a complex design.

By taking advantage of the positive attributes, we have chosen to devote this project to further investigate and advance some metrological aspects of the magnetic zero-flux technique, which has been utilized for many decades and there exists a number of manufacturers providing commercially available systems with somewhat different features. The challenge behind this study is to through practical laboratory tests create a picture of how one of these solutions performs at frequencies well above for what it was optimized.

As current measurements serve in general various purposes, different requirements are therefore set on them. These are different if the application is for example a continuous monitoring in a power grid, finely tuned methods for research and development, or certified methods applied for calibration and accreditation. If the development of a measurement technique aims for a specific application, there are often well determined requirements concerning the desired ranges and measurement uncertainty. However, as measurement techniques themselves are ideally generic, they can be utilized within a vast range of other applications. This project thus aims at bringing up some vital issues for optimal utilization of zero-flux technique, within unspecified application field of AC current measurements. The applicability of the findings will be different depending on the application. Practical laboratory tests on a state-of-art zero-flux system are used to create a picture of its properties at higher frequencies than its manufacturer has provided detailed specifications for.

In the research conducted in this study, focus has been put on determining how sensitive the measurement results are to practical arrangements and limitations of the measurement setup. Hence, this work provides a method and guide to assess how different configurations of the measurement setup affect the measured results in different frequency ranges. Among the aspects identified in this work as significant are: (i) identifying the source of the measurement error in the zero-flux system's design and, if possible, minimizing this error , (ii) the measurement error and the measurement uncertainty of a zero-flux system in a presence of geometric by design adjustments asymmetry of the cabling and disturbances brought up by return, or nearby located, conductors, (iii) simultaneous measurements of sinusoidal signals of different amplitudes, frequencies and phase angles, (iiii) detection of sub-synchronous events, and (v) non-steady state phenomena, like for example transients in the drive line of electrical vehicles. The first two aspects are mainly elucidated, but some conclusions can also be drawn as concerns the latter.

Reduced measurement accuracy due to the disturbance brought up by nearby located electrical conductors is a fact in almost all practical installations, both in and outside of laboratory environments. The magnetic field induced in a zero-flux sensor, or in any current transformer sensor, stem from all currents flowing within a certain distance from it, i.e. from the primary current conductor, whose current should be measured, and from conductors disturbing the measurement. It is thus impossible to distinguish the origin of all the sources of magnetic field, which will bring up measurement errors. Furthermore, in many practical three-phase installations, the three current conductors are located close together. The magnetic fields generated in the two nearby conductors are 120 and 240 degrees out of phase, but can influence the operating point in the examined magnetic core. Manufacturers of zero-flux measuring systems specify the minimum distance to other current conductors. However, quantification

of the errors arising in specific arrangements remains the task of the end users. A study of this phenomenon is essential for on-site calibrations of lower precision measuring systems.

Concerning measurements of currents containing harmonic components or transient phenomena, evidences for the presence of current harmonics in power grid installations [7] and [8] are well documented. Among the undesired effects of current harmonics is for example appearance of neutral currents in three-phase wye connected AC systems [9], yielding excess loads in transformers [10] and [11].

Presence of sub-synchronous resonance is also possible [12], [13], and known to occur for example in networks with series-compensated transmission lines and wind farms [14]. The zero-flux technique facilitates detection of such low frequency phenomena and therefore provides means of early warnings, which may prove useful in monitoring wind farm installations. Some results from zero-flux measurements down to 5 Hz are therefore reported here as well, but are not the focus in this work. Transients can be caused by components in the grid itself, like for example switching operations, or lightning strokes. The current transients are often rapidly damped, but have been reported to cause damage to LED-lamps in street lightning [15].

1.3 Thesis outline

Chapter 2 elaborates on the motivation for the choice of the zero-flux technique and describes its basic operation principles.

Chapter 3 describes the experimental setup, including the DSWM technique being the measurement evaluation principle of this work.

In ***Chapter 4***, the zero-flux system is considered from a system's perspective, conceptually split into different functionalities, i.e. the magnetic circuit, the feed-back system and the read-out buffer. The measurement error of the system and its behaviour is determined, including the errors brought up by components from the respective parts, and the results of this investigation are used for improving system's performance at frequencies in the kHz range. A ratio of phase angle error to frequency, $\Delta\varphi/f$, is proposed to be used as a characteristic quantity for comparing zero-flux systems.

As any magnetic sensing system responds to asymmetric distribution of the magnetic field and the effect tends to worsen as the frequency increases, ***Chapter 5*** provides a thorough analysis on how changes in geometrical arrangements of the primary current loop affect the measured output from the zero-flux system. The geometrical parameters investigated are: de-centring of the primary conductor, parallel and perpendicular distances to the return conductor, as well as sensor rotation and its tilt. This chapter can either be utilized as an inspiration for how to design a new measuring setup or, if a similar setup to the one described in this thesis is used, to find error levels at certain frequency ranges.

Chapter 6 summarizes the conclusions from this work.

Chapter 7 provides suggestions for the continuation of this work.

1.4 List of publications

[1] M. Hammarqvist, A. Elg, A. Bergman, J. Blennow and S. M. Gubanski, "Investigation of the Frequency Dependency of Phase Angle Error in a Zero-Flux Current Measuring System", in *Int. Symp. on High Voltage Engineering* , Seoul, Korea, 2013, p. 525.

[2] M. Hammarqvist, A-P. Elg, A. Bergman, J. Wolbert, J. Blennow and S. M. Gubanski, "Improvement of Frequency Response for a Zero-Flux Current Measuring System", in *Conf. on Precision Electromagnetic Measurements*, Rio de Janeiro, Brazil, 2014, pp. 618-9.

[3] M. Hammarqvist, A-P. Elg, A. Bergman, J. Blennow and S. M. Gubanski, "Improvement of Frequency Response for a Zero-Flux Current Measuring System", submitted for publication to IEEE Transactions on Instrumentation and Measurement, revision in progress.

2 Non-contact current measurement techniques

2.1 Background

FOR measurements of electric currents, accurate methods are well described in applications referring to high current/low frequency, for example [16], [17], and to low current/high frequency ranges, for example [18], [19]. However, there is still a need for further development of traceable measurement methods capable of handling high frequency components superimposed on DC or power frequency currents in the kA range, which is the level relevant for the transmission and distribution grids. Due to limitations in the available equipment, the main current here however had a maximum of 100 A. The amplitudes of the high frequency components, being limited by circuit inductances, are relatively small compared to that of the main current, and the methods must therefore be characterized by sufficient resolution. A central feature of a traceable method is therefore existence of a measuring system capable of handling such differences.

A number of non-contact techniques for measurements of electric currents are utilized in practice. We introduce here briefly the most common ones, i.e. current transformer (CT), in its original and its refined state known as magnetic zero-flux CT, Rogowski coil and Pearson coil. In addition to the ordinary current transformer, which utilizes magnetic coupling, there are also non-conventional current transformers, like for example the optical current transformer, utilizing Faraday Effect [20], [21].

The measurement error of a current transformer is directly related to the magnetization of the core and to obtain precise measurements minimizing its magnetization is required. The technique allowing to cancel out the magnetic flux of the core is the zero-flux technique, in which a feedback circuit is used to create a balancing compensating current. This compensating current is proportional to the measured primary current and it can either be measured directly or be fed into an instrument amplifier connected through a shunt resistor. The underlying principles of the technique are thoroughly described in [22], also containing relevant references to the early work, for example [23].

A technical area where great advances have been achieved regarding the zero-flux technique is the monitoring and control of particle beams [24], [25], especially regarding the measurement of DC with ppm accuracy [26]. For wide-band applications, claims are made of DC – circa 1 MHz and measurement uncertainties of around 1% [27], [28].

Unlike the traditional current transformers as well as Rogowski and Pearson coils, which allow measuring only AC currents, the zero-flux technique enables simultaneous measurements of AC and DC currents, sub-synchronous events and non-symmetrical curve forms. The latter case includes for example impulse phenomena occurring when large inductive loads are added to the grid. Regarding the high frequency range, the zero-flux technique is limited by the properties of core material, just like the current transformer is. In this study Fe-Si cores are used, but for wide-band characteristics, amorphous cobalt-based cores can be utilized. For the very high frequencies, the manufacturer Bergoz claims a cut-off frequency of up to 2 GHz, but the search for scientifically proven accuracy of these solutions has been unsuccessful.

In a Rogowski coil [29], [30], [31] a time-varying magnetic field induces a voltage proportional to the time derivative of the current, resulting in a non-linear frequency response. Although the bandwidth is superior to that of a conventional zero-flux sensor, the measured output will be affected by the magnetic environment around the sensor [32], for example positioning of the sensor around the current conductor [33]. On-site calibration in a 400 kV substation utilizing Rogowski coil has been performed with a measurement uncertainty of 300 μA/A [34].

The Pearson coil, sometimes referred to as self-integrating Rogowski coil, can be considered as a synthesis between the current transformer and the Rogowski coil. Due to its excellent sensitivity to high frequencies, it can be utilized for impulse current measurements [35]. Claims are made for its usability in the ns range [36] and [37], but it still has a limited accuracy, partly due to core saturation that yields a distorted wave form. The Rogowski and Pearson coils respond only to AC currents.

As a possible continuation of this work is to achieve a traceable measurement method for high electrical DC and power frequency currents with superimposed high-frequency components, utilizing a zero-flux current measuring system seems to be a natural choice. Development of such a method includes evaluation of the zero-flux system abilities as well as further exploration of its measuring characteristics. This exploration refers to an extension of the nominal frequency range of the system and its characterization above this range under ideal and externally disturbed conditions. It also refers

to investigation of the impact that positioning of the zero-flux sensor has on the measurement error and the measurement uncertainty. The zero-flux measuring system was also evaluated before and after introduction of two minor changes in the electronic circuitry for improving its frequency characteristics.

2.2 Zero-flux technique

2.2.1 Basic principle for AC

The main component in the zero-flux technique for AC current measurements is a magnetic integrator, as illustrated in Figure 2. It consists of a toroidal ferromagnetic core, placed around the primary current conductor, equipped with a secondary winding, N_{sec}, and an auxiliary winding, N_a. The primary current to be measured induces a flux in the toroid, which in turn induces a voltage in the auxiliary winding. The auxiliary voltage is fed into an integrating power amplifier that injects a current in the secondary winding, which induces an opposing flux in the core. Any remaining flux will be sensed by the auxiliary winding N_a and affect I_{sec} until a stable condition is achieved when the fluxes generated by I_{prim} and I_{sec} exactly cancel out, i.e. the zero-flux condition is fulfilled.

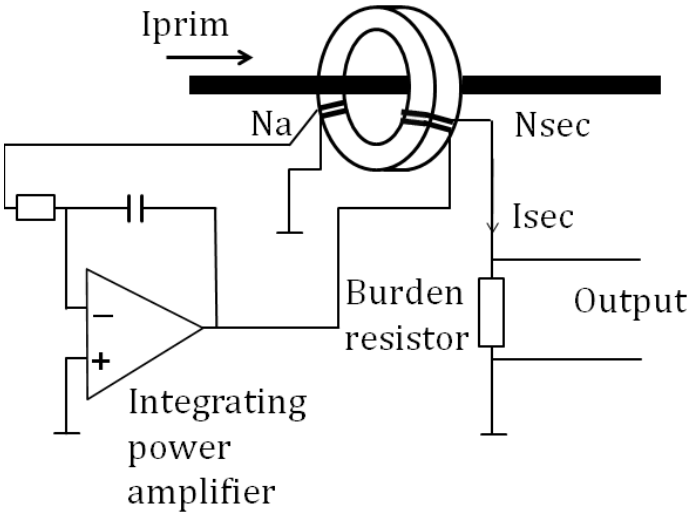

Figure 2: Schematic view of magnetic integrator in AC zero-flux measuring system.

The current in the secondary winding I_{sec}, is hence the measure of the primary current I_{prim} via the turns ratio of N_{sec}, as it is the current required to eliminate the flux generated by I_{prim}. I_{sec} is most conveniently measured as the output voltage over a burden resistor. Only a time-varying magnetic flux can induce a stable current in a secondary winding, hence this principle works only for AC.

2.2.2 DC measurement principle

To form conditions for additionally measuring DC currents, a three toroid zero-flux system, including both DC sensing cores and the magnetic modulator, has been introduced. It is shown in Figure 3.

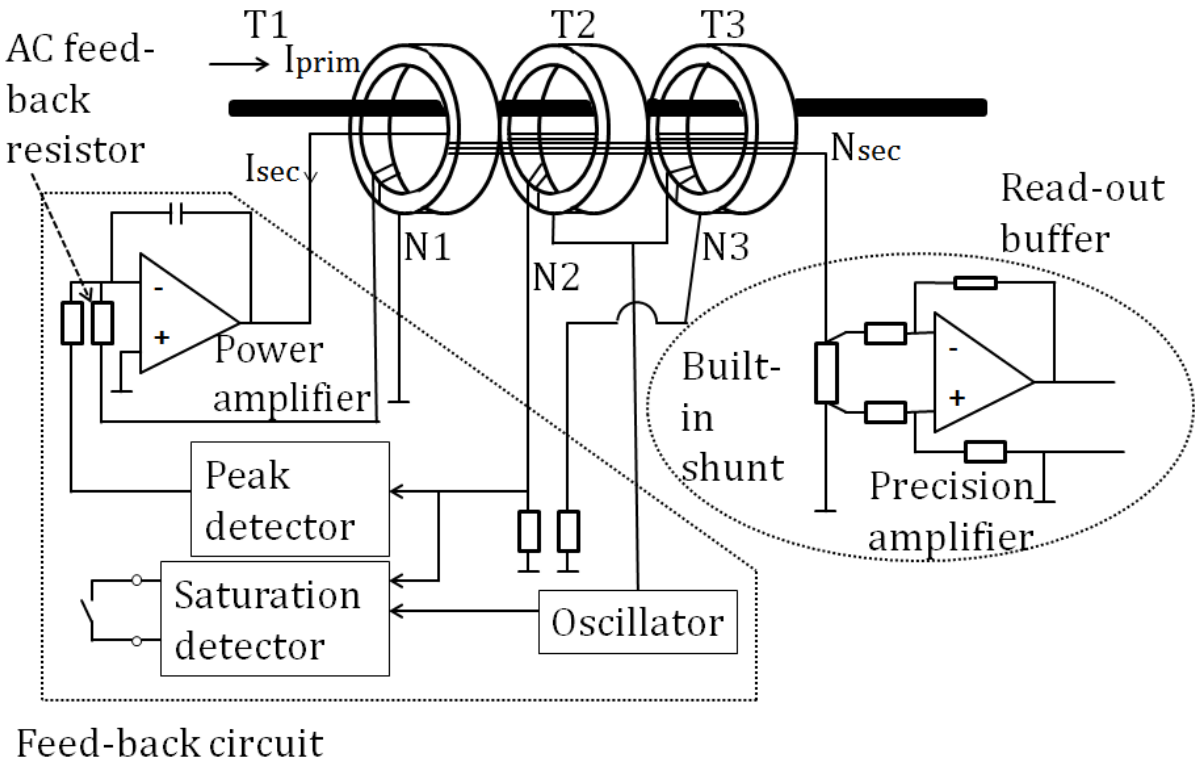

Figure 3: Schematic view showing the main principle for AC and DC zero-flux measuring systems.

The three toroid zero-flux system of Figure 3 combines the magnetic integrator core (T1) and two additional toroidal cores (T2 and T3), utilized to measure DC. The two DC sensing cores are driven to saturation in opposite directions by a square-wave oscillator. The difference between the resulting current peaks in N2 is zero if no current flows in the primary conductor, and the integral output from the power amplifier is hence also zero. Core T3 is required to avoid injection of the oscillator frequency into the main circuit. When DC current flows in the primary conductor, the current through the N2 winding will be asymmetric and the peak detector will provide a feedback signal to the power amplifier that is proportional to the DC flux. The control loop will now tune the secondary current for achieving the zero-flux condition. More details on the exact function of the zero-flux technique for AC and DC can be found in for example [38], [39] and [40].

2.3 Quantities characterizing a zero-flux system

A pure sinusoidal AC current is characterized by its amplitude, frequency and phase angle relative to a reference. A measuring system determining the current amplitude and its phase will always introduce errors, an amplitude error and a phase angle error, and when characterizing any AC measuring system, both need to be determined. Instead of amplitude error, one can also make use of a scale factor for the amplitude, SF, which is defined as the value by which the measuring system output quantity must be multiplied to obtain the true value. For a zero-flux measuring system with a voltage output, the relationship is expressed as $I_{prim} = SF \cdot V_{output}$. Obtaining the correct values of SF and phase angle error $\Delta\varphi$, including the measurement uncertainty, is always a time-consuming and often multistep

procedure, where input level dependency, frequency and ambient conditions, such as temperature, humidity and sensitivity to external disturbances, must be taken into account.

The frequency dependence of the aforementioned errors shows variations between different frequency regions, due to different operating modes; the DC operating mode, the active AC compensation mode and the passive AC mode (high frequencies). In the DC operating mode (DC and low AC frequencies), the DC circuitry is operational and establishes the zero-flux condition and the frequency dependences of the errors tend to be hard to predict and can be quite different for different measuring systems. In the passive AC mode, the errors increase rapidly with increasing frequency. In contrast, in the active AC compensation mode, where the AC feed-back system is operational, there is however a large frequency span in which the frequency – SF relationship is more or less constant and the frequency – phase error relationship is linear. Dividing the phase error, $\Delta\varphi$, measured in radians, by the frequency yields a more or less constant value and this quantity $\Delta\varphi/f$ (expressed in μs) is a convenient and characteristic factor describing zero-flux system quality. It will thus be used henceforth in this work. Transition regions can be detected between the operating modes and these regions will be further elaborated on below.

3 Experimental setup

3.1 Overview

THE experimental setup used in this work consists of an AC current source feeding two measuring systems; the zero-flux system under test and a reference measuring system. A voltage is generated by a high-performance calibrator in the AC current source, feeding its signal to a wideband transconductance amplifier, which in turn generates a primary current in the range 2 – 100 A and frequency 10 Hz – 250 kHz. The maximum frequency for a given current and, reversely, the maximum current for a given frequency are limited by the size and the geometry of the primary current loop, i. e. the load inductance sensed by the transconductance amplifier. The primary current is supplied to the measuring systems through a coaxial arrangement, depicted in Figure 4, with the purpose to minimize the circuit inductance.

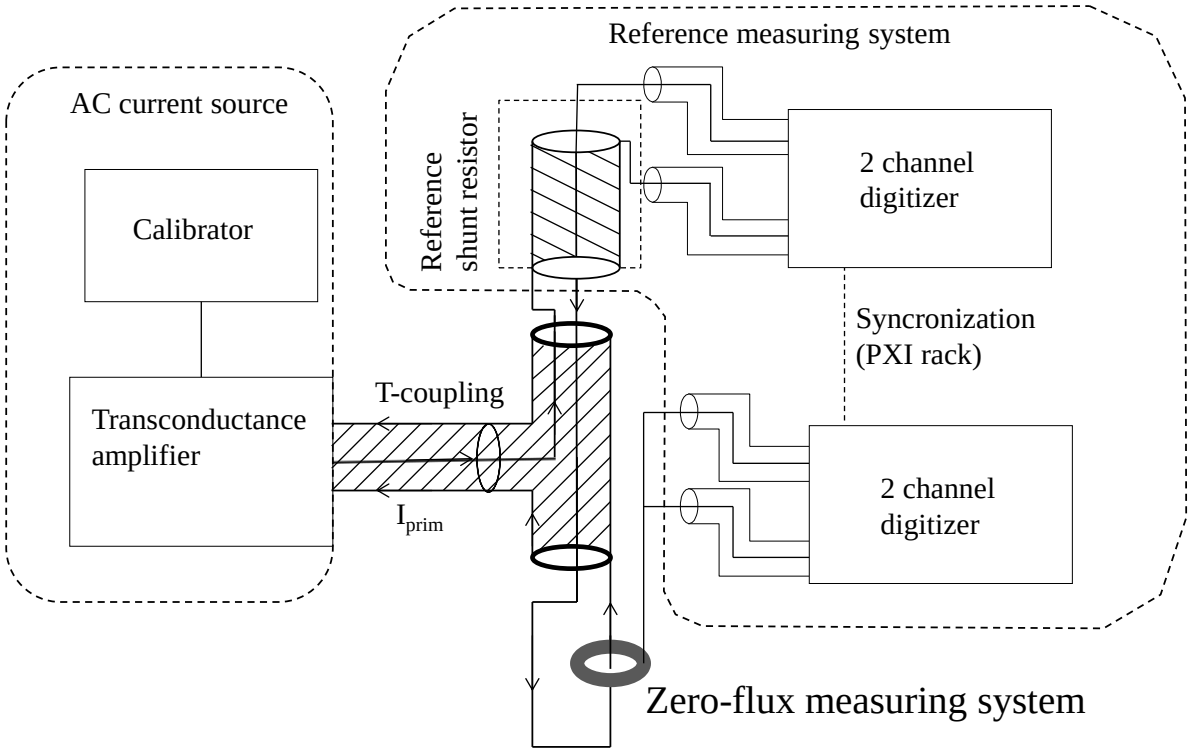

Figure 4: Schematic view of the measurement setup. The reference shunt resistor is of coaxial design.

3.2 Coaxial current arrangement

The T-coupling (central in Figure 4) is a crucial component in the setup. It provides a low load inductance and a serial path of the primary current through the two measuring systems. The inductance is minimized in this arrangement by bidirectional path of the primary current. However, the arrangement is truly coaxial in its central and lower arm only, whereas in the upper arm the downward current and the upward current travel in two parallel wires. This will certainly create a difference to be sensed by the digitizers of the reference measuring system. The length of the two symmetrical arms in the T-coupling should be as small as possible for minimizing the measurement error brought up by the capacitances of the arms. Two different T-couplings were utilized in the reported measurements, the capacitance difference in the two arms was below 1 nF for the results reported in Chapter 4 and below

0.1 nF for the results reported in Chapter 5. The inductance differences are too small to have any practical influence on the reported results.

A coaxial current path around the zero-flux system, although possible to arrange, is not implemented in this work since the resulting setup would be too different from what is practically used. The geometry of this part will thus considerably change the load inductance, thereby causing the supplied current to drop somewhat as the load increases. Despite of this, because of using both the tested and the reference measuring systems simultaneously, a need for stable current source is eliminated.

3.3 DSWM reference measuring system

A Digital Sampling Watt Meter system (DSWM) [41] was utilized as the reference measuring system. The DSWM is a two channel digitizer for power measurements and its operation principle is based on "the equally-spaced, simultaneous sampling of voltage and current during an exact number of periods of the fundamental frequency" [41]. Figure 5 illustrates components of DSWM system.

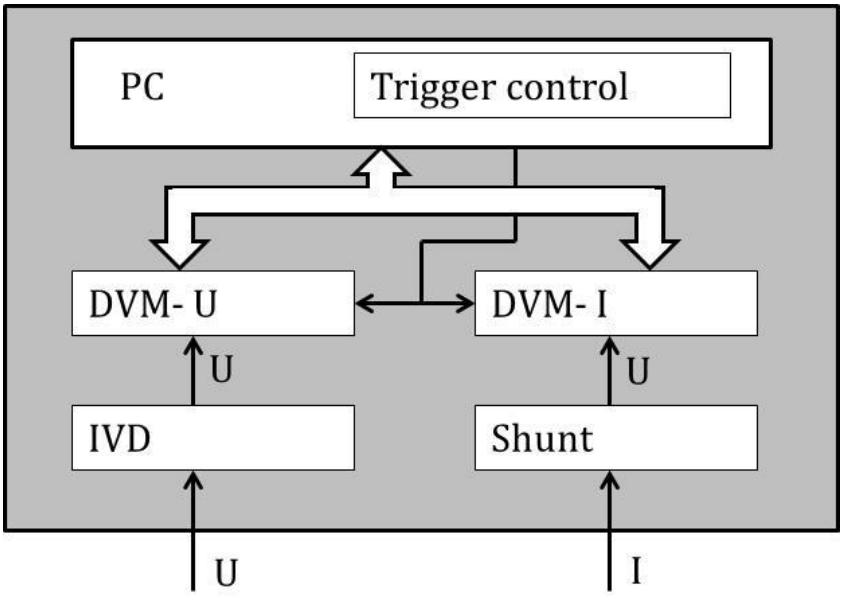

Figure 5: Schematic principle of Digital Sampling Watt Meter. IVD stands for Inductive Voltage Divider, DVM-U and DVM-I are digital voltmeters for voltage and current measurements.

Outputs of the two DSWM channels provide voltages at easily measured levels and for achieving this condition, a precision coaxial shunt must be used in the current channel and a precision voltage divider in the voltage channel. It is also possible to measure two currents or two voltages and in this work the former option was adopted.

To cover a frequency range as broad as possible, two different DSWM systems, DSWM 1 and DSWM 2, were utilized. The operating principle of the two systems is exactly the same, but different digitizers are utilized. DSWM 1 [42] utilizes two 8½ digit multimeters in DC mode and has a measurement range of 5 Hz – 3.5 kHz, measurement uncertainty better than 40 µV/A and 40 µrad at 50 Hz. A phase-locking unit ensures simultaneous measurement of the two channels, implying that also the phase angle difference between the two signals can be measured. The second reference system, DSWM 2 [43], [44] has a measurement range of 10 Hz – 1 MHz, measurement uncertainty better than 60 µV/A and 60 µrad at k = 2 and 50 Hz. It utilizes high quality AD-converters communicating by means of internally synchronized PXI-cards. More details about both DSWM systems are provided in Table I.

Table I. Parameters of DSWM systems used in this work

	Nominal frequency range	Measurement uncertainty SF	Measurement uncertainty Phase angle error
DSWM 1	5 Hz – 3.5 kHz	40	40
DSWM 2	10 Hz – 1 MHz	60	60

3.4 Reference measuring shunt

The reference measuring shunt was a 100 A DSWM shunt, Figure 6, Its characteristics are ensured by in-house calibrations up to 1 MHz. For example, DC power dependence of the shunt, here defined as the difference in DC resistance after a 30 minutes warm-up time between 100 % and 50 % of nominal current, is equal to -15 μΩ/Ω. This corresponds to -20 μΩ/Ω for a current change of 0 % - 100 %. As in the work presented below the measurements were taken at random times after application of the current, without allowing the warm-up time, the power dependence uncertainty of maximum 20 μΩ/Ω was considered. As regards the frequency dependence, the AC-DC difference in resistance of the shunt is typically -30 μΩ/Ω below 100 kHz (within -20 μΩ/Ω below 10 kHz), whereas the AC power dependence at 100 kHz is within 10 μΩ/Ω.

In this work, the measurement uncertainty of the reference measuring shunt was negligible in comparison to the other error sources. For a complete traceability additional analyses are needed, but this has not been the focus of the reported work.

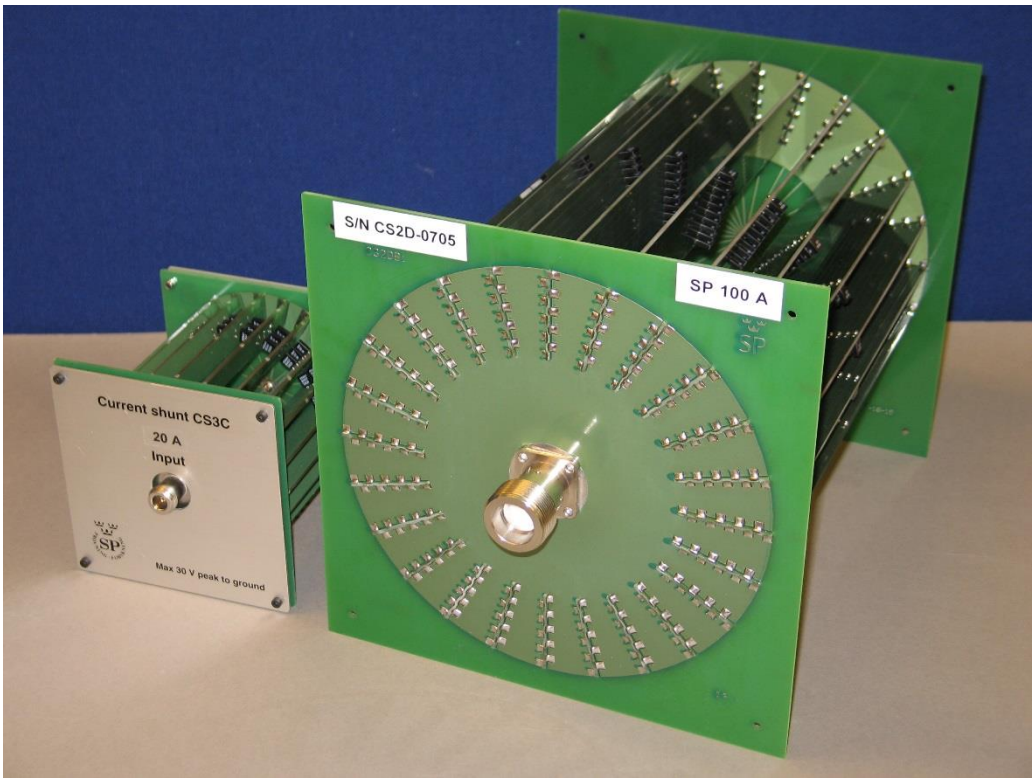

Figure 6: Example of DSWM shunts. Several different shunts with nominal currents between 200 mA and 100 A exist. In this work the 100 A shunt to the right was utilized.

3.5 Devices Under Test (DUT)

Three different types of zero-flux systems were utilized, defined in the following as Devices Under Test (DUTs). They all have the same basic design, described in more detail in Chapter 4, with a measuring head consisting of ferromagnetic cores, secondary and auxiliary windings, an interconnecting cable and an electronic unit, as illustrated in Figure 7 and Figure 8, the interconnecting cable carrying the zero-flux control current, which also is the quantity to be measured. The reason for working with different systems, some of them being of older design (not fully documented), is that we aimed at generalization of measurement principles rather than at optimization of one specific construction and the outcomes should be applicable to any zero-flux system of similar general design.

The system types used were thus an improved standard accuracy (StAcc) system (1 unit) [38], a top accuracy (TopAcc) system (2 units) [39] and the SUM system (1 unit) [40], the latter being two StAcc systems built into the same box. The top accuracy of the TopAcc system refers to its DC accuracy, whereas the AC accuracy, which is of interest in this investigation, remains the same as for StAcc one. The respective nominal scale factors SF were 2000A/10V for TopAcc system, 600A/10V for StAcc system and 500A/5V for SUM system. The systems are designed to measure mainly up to their rated currents at DC and AC below 1 kHz, even though a bandwidth of up to 100 kHz is specified by the manufacturer. However, above 1 kHz a de-rating of the current is recommended for avoiding overheating. Hence, at frequencies above 20 kHz, the maximum recommended current is 5 % of the rated current. As already mentioned, the referred systems are in the following labelled as DUT followed by a number. DUT 1 and DUT 2 are both of TopAcc type, DUT 3 is the SUM system and DUT 4 is the StAcc system.

The outer diameter of the core in Figure 7 (StAcc, type 600LHC) is 8 cm, the diameter of the hole is 3.5 cm and the side length of the quadratic cross area is 3.5 cm.

The outer diameter of the TopAcc system cores (including housing) is 12 cm, the diameter of the holes is 4 cm and the side length of the quadratic cross areas 7 cm.

The outer diameter of the core in Figure 8 (SUM, type 2ST20) is 11 cm, the diameter of the hole is 5.2 cm and the side length of the quadratic cross area is 5.5 cm.

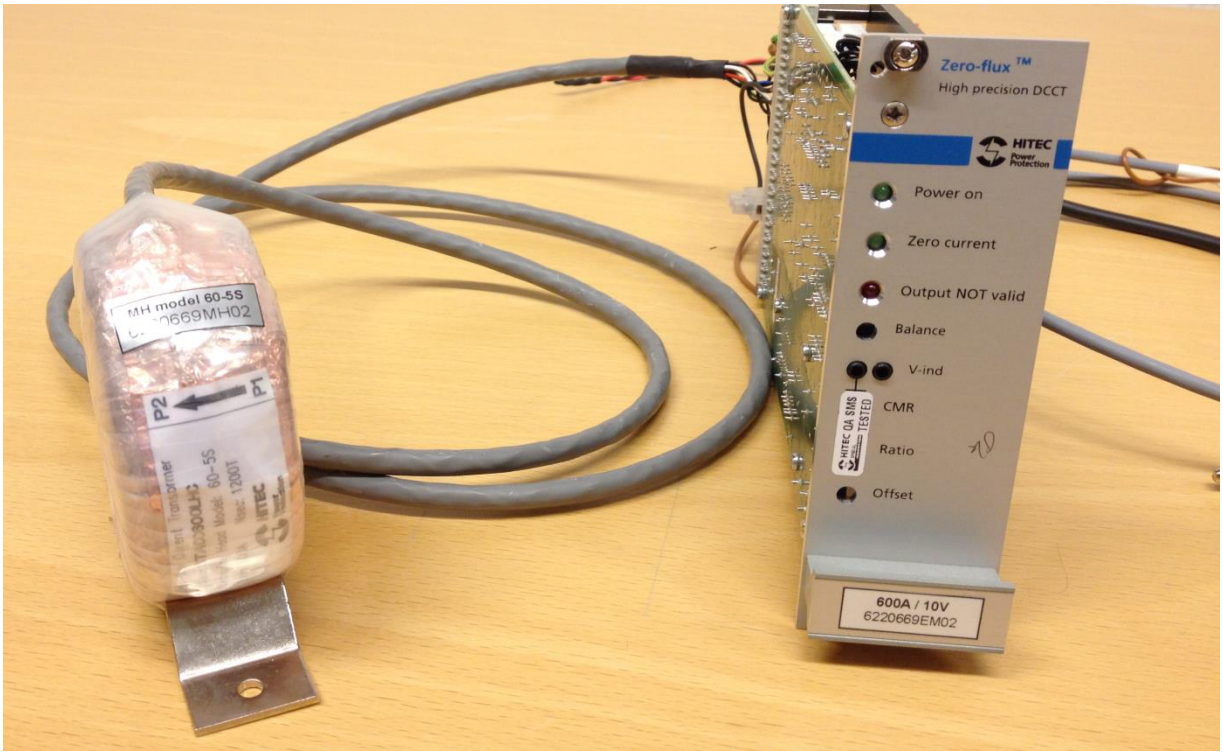

Figure 7: Photo of 600A/10V StAcc (type 600LHC) system.

Figure 8: Photo of 500A/5V SUM (type 2ST20) system.

3.6 Measured and calculated quantities

A short account for the derived quantities is now provided. The DSWM system measures the voltage ratio:

$$Measured\ ratio = \frac{V_{DUT}}{V_{ref}}$$

where $V_{DUT} = V_{output}$ is the voltage output of DUT, V_{ref} is the voltage output of reference

and the phase angle error $\Delta\varphi$:

$$\Delta\varphi = \varphi_{DUT} - \varphi_{ref}$$

where φ_{DUT} is the phase angle of DUT output voltage and φ_{ref} is the phase angle of reference output voltage. The latter is set to zero, and thus the measured phase angle error is fully attributed to the phase shift introduced by the zero-flux system.

In addition, the scale factor SF is defined by:

$$SF = \frac{V_{DUT}}{I_{prim}}$$

and

$$V_{ref} = R_{shunt} \cdot I_{prim}$$

As the zero-flux system and the reference DSWM shunt are placed in series in the primary current loop, measuring the same primary current, the measured ratio will be:

$$Measured\ ratio = \frac{SF \cdot I_{prim}}{R_{shunt} \cdot I_{prim}} = \frac{SF}{R_{shunt}}$$

The measured ratio is hence directly proportional to the scale factor of the zero-flux system, assuming that R_{shunt} is constant. The DC resistance of the shunt at full current (100 A) is $7.99631 \cdot (1 \pm 4 \cdot 10^{-6})$ mΩ and at 50 A, $7.99619 \cdot (1 \pm 4 \cdot 10^{-6})$ mΩ.

4 The zero-flux technique from a system's perspective - characteristics and improvements

SYSTEMS based on the zero-flux technique are commonly utilized current measurement devices, especially when high accuracy measurements are needed. To achieve correct measurement results, including the measurement uncertainty, one crucial factor is the knowledge of and accountancy for the phase angle error introduced by the zero-flux system itself. For practical reasons, it is also desirable to minimize this error.

One practical example of measurements, where knowledge of the phase angle error is important, is electric power measurements, especially with power factors close to zero, $\cos\varphi = 0$, where a small angular error will greatly influence the correctness in the measured active power. Another example is calibration of reference transformers, where the phase angle error is determined together with the amplitude error as part of ensuring its classification.

This chapter has two purposes: One is to establish a generally applicable method for the minimization of the phase angle error of a zero-flux system, by first identifying its conceptual origin in the design as such; the other is to gain confidence in the evaluation method, by comparing two reference systems utilizing a zero-flux system as transfer standard. First, measurements are presented showing that the largest contribution to the phase angle error stems from the electronic unit, [45], and then measurement results from two different adjustments to the electronic unit, serving to improve the high frequency characteristics are presented. Finally a comparison between the two DSWM systems with different frequency ranges is presented; the traditional DSWM system, henceforth referred to as DSWM 1, with nominal measuring range 5 Hz – 3.5 kHz and DSWM 2, with nominal measuring range 10 Hz – 1 MHz. In the frequency range where the two DSWM systems overlap, a comparison between the two systems is made [46]. The scale factor of the system investigated in this chapter was 100 A/V, and the SF results are presented as A/V.

4.1 The zero-flux system revisited

To determine the origin of the phase angle error from a system's perspective, a rough but useful model is to regard the zero-flux measuring system as a magnetic circuit, a feed-back system, and a read-out buffer (Figure 9). In the zero-flux systems in this study, the feed-back system and the read-out buffer are physically located in a separate electronic unit.

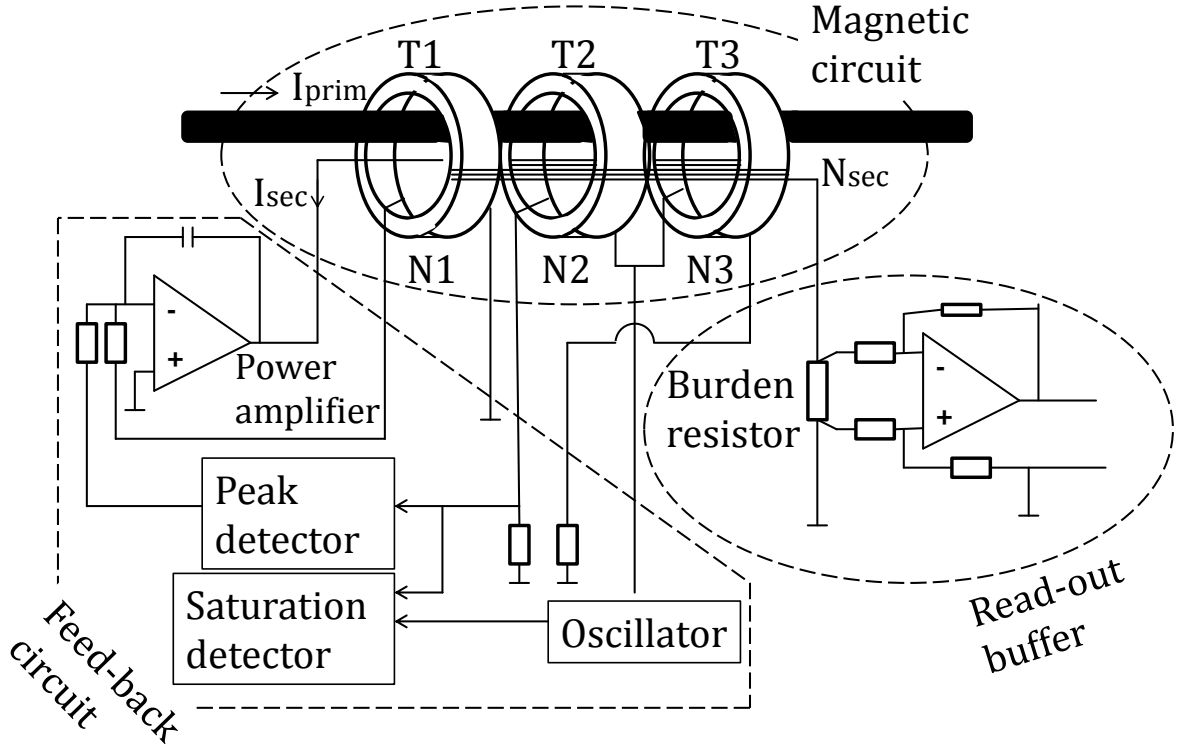

Figure 9: The zero-flux system divided conceptually, according to functionality.

The determination and minimization of the phase angle error of a zero-flux measuring system in the frequency range 5 Hz – 100 kHz will now be described. Three different zero-flux systems described in section 3.5 were utilized; DUT 1 and DUT 2 were investigated to identify the conceptual origin of the phase angle error, and the newer DUT 3 system was adjusted for the minimization of the phase angle error. By not limiting the investigations to one specific instrument type, or even one specific individual, we gained increased confidence in the general applicability of the findings. The utilized method is generally applicable.

4.2 Determination of errors

The system in Figure 9 is sectioned according to functionality; magnetic circuit, feed-back circuit and read-out buffer. The latter consists of a burden resistor and a precision amplifier. The methodological approach was to identify from which part of the zero-flux system the major errors origin, and to quantify the errors.

First, the phase angle error of the complete zero-flux system in normal operation, V_{out}, was measured. Secondly, the secondary current path was opened, and the current was fed through a well characterized external AC current shunt, and the phase angle error of this signal was measured. This removes the error component introduced by the read-out buffer, and gives the error of the active transformer (magnetic circuit and feed-back system). In both cases, the reference signal was the primary current measured over a high-performance AC current shunt as presented in section 3.3. Thirdly, V_{out} was measured using the secondary current as reference signal. The system is still fed by the primary current and the internal compensation system is in operation. Hence, the measured error now originates from the read-out buffer alone.

The integration of the burden resistor and the precision amplifier in the read-out buffer made it impractical to separate the errors stemming from these. When measuring the output signal with an external shunt, the read-out buffer was not removed, thereby the burden in the circuit was changed, but

still within the manufacturer's specification. The feed-back system was always operational, so the exact parameters of the magnetic circuit in its stand-alone mode were not determined.

Now the complete zero-flux system was fed by a sinusoidal 10 A rms current and V_{out} was measured. Figure 10 and Figure 11 show the phase angle errors of DUT 1 and DUT 2 respectively for the full system, the active transformer, the electronic unit, and the calculated sum of the contributions from the active transformer and the electronic unit. DSWM1 was utilized as reference system.

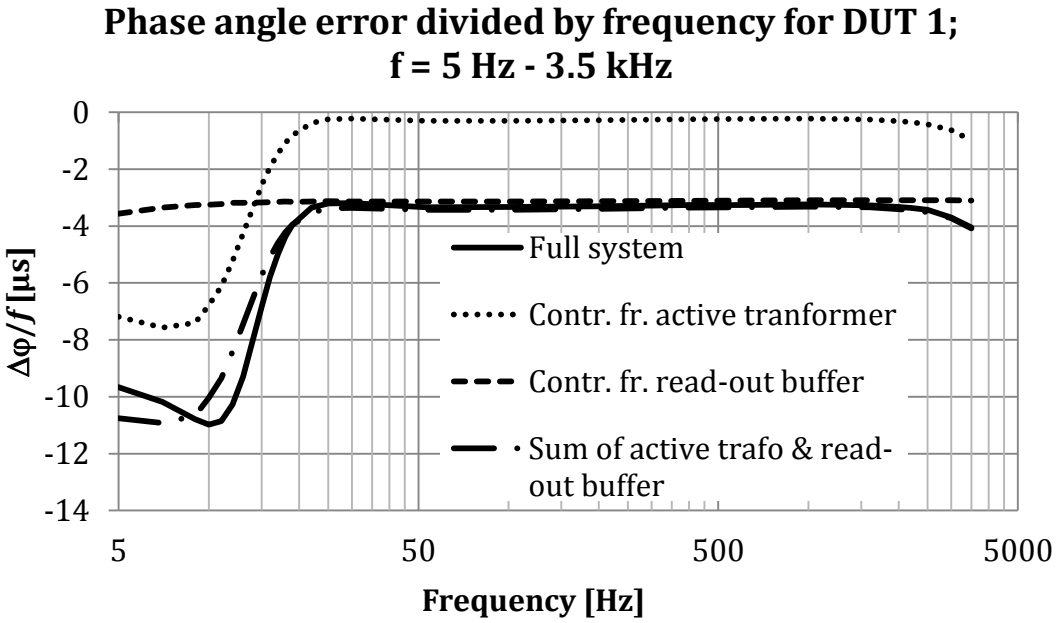

Figure 10: Phase angle error $\Delta\varphi/f$ as a function of frequency for 5 Hz to 3.5 kHz for DUT 1 using DSWM1 as reference system.

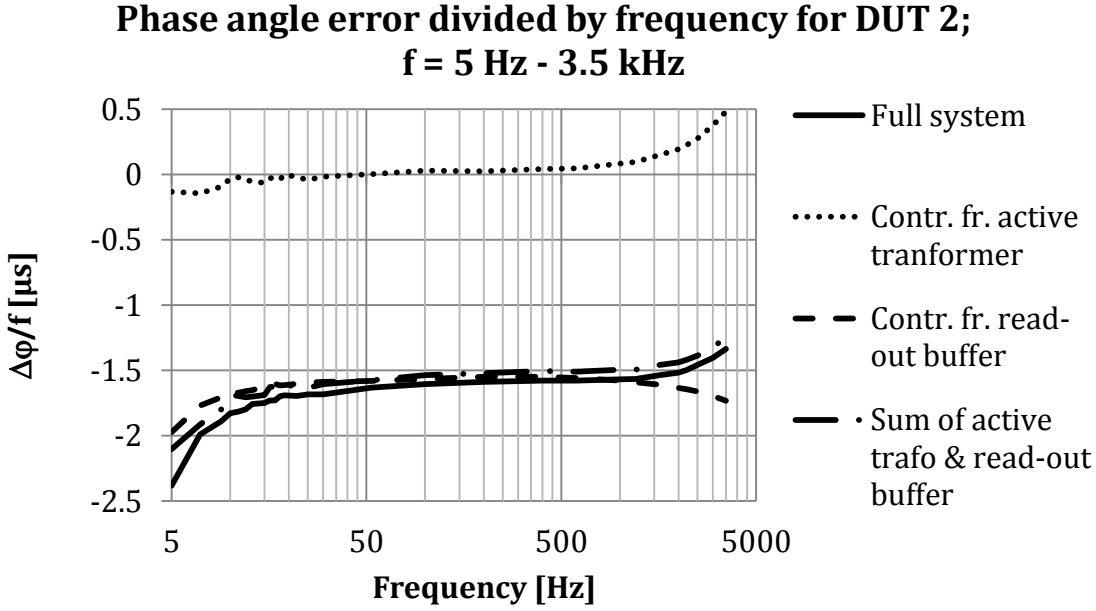

Figure 11: Phase angle error $\Delta\varphi/f$ as a function of frequency for 5 Hz to 3.5 kHz for DUT 2 using DSWM 1 as reference system.

If the calculated sum of the contribution from the active transformer and the read-out buffer coincides with the measured error of the full system, within the measurement uncertainty of DSWM 1, this would serve as a proof that the conceptual sectioning of the zero-flux system introduced above is accurate and useful as a model in the efforts to improve the high-frequency characteristics of a zero-flux system.

4.2.1 Comparison of errors and reference system uncertainties

The sum of the measured contributions from electronic unit and active transformer (henceforth referred to as Σ) coincide with the measurements of the full system (F) (Figure 10 and Figure 11). This will now be quantified more in detail. A comparison of the difference Σ - F and RISE's CMC (Calibration and Measurement Capability) entries for the DSWM systems will be made. The CMCs are, as mentioned earlier, the best achievable measurement uncertainty for a certain method, in this case the DSWM system. For a complete measurement uncertainty analysis, factors from the rest of the measurement setup, as well as the standard deviation of the performed measurement series must be included. Since a formally correct and complete measurement budget was not the focus of this work, we have settled for a comparison to the CMC values. If Σ - F is of the same magnitude as the CMC, it will be considered as sufficient confirmation for conformity between the two DSWM systems. The CMC for measurement of phase angle error with the DSWM systems is given by [47], reproduced in Table II.

Table II. CMC entries for measurements performed with DSWM. The expanded uncertainties are expressed in mW/VA, which will translate to the same numbers for phase angle error expressed in μrad (utilizing the approximation that tanθ = θ for small values of θ), and for amplitude [47].

		10 Hz	60 Hz	1 kHz	10 kHz	20 kHz	30 kHz	50 kHz	100 k Hz
1 - 20 V	5 mA – 2 A	0.13	0.12	0.12	0.2	0.4	0.6	1	2
	2 – 20 A	0.13	0.12	0.12	0.2	0.4	0.6	1	2
	20 – 100 A	0.13	0.13	0.13	0.3	0.6	0.9	1.5	3
20 - 200 V	5 mA – 2 A	0.13	0.12	0.12	0.2	0.4	0.6	1	2
	2 – 20 A	0.13	0.12	0.12	0.2	0.4	0.6	1	2
	20 – 100 A	0.13	0.13	0.13	0.3	0.6	0.9	1.5	3
200 – 600 V	5 mA – 20 A	0.14	0.13	0.13	0.3	0.6	0.9	1.5	3
	20 – 100 A	0.14	0.14	0.14	0.35	0.7	1	1.6	3.2

As mentioned earlier, $\Delta\varphi/f$ is in this study utilized as a quantity characteristic to the zero-flux system. With $\Delta\varphi$ expressed in μrad and f in Hz, the CMC for $\Delta\varphi/f$ is calculated as the CMC entry for the phase angle error divided by the frequency. The CMC for $\Delta\varphi/f$ in the present measurement situation is given by Table III.

Table III. Expanded measurement uncertainties, expressed in μs, for phase angle error divided by frequency, calculated from the CMC entries for DSWM.

		10 Hz	60 Hz	1 kHz	10 kHz	20 kHz	30 kHz	50 kHz	100 k Hz
1 - 20 V	2 – 20 A	13	2	0.12	0.02	0.02	0.02	0.02	0.02

For 10 Hz – 1 kHz, DSWM 1 gives the best measurement uncertainties and hence the CMC, and above 1 kHz, DSWM 2 takes precedence. In Table IV, the CMC entries are given for some chosen frequencies, together with the difference Σ - F for DUT 1 and DUT 2.

Table IV. CMC entries for DSWM, and Σ – F (sum of contributions from read-out buffer and active transformer minus phase angle error of full system) for DUT1 and DUT2.

Frequency [Hz]	CMC for $\Delta\varphi/f$ with DSWM [μs]	DUT 1 Σ - F [μs]	DUT 2 Σ - F [μs]
10	13	0.14	0.95
60	2	0.06	-0.09
1000	0.12	0.07	-0.07
2000	0.06	0.08	-0.08
3000	0.04	0.08	-0.08
3500	0.043	0.09	-0.04

Below 1 kHz the difference Σ - F is well within the CMC of DSWM 1 for both DUT 1 and DUT 2. Above, Σ - F is of the same order of magnitude and sometimes larger than the CMC of DSWM 1, but it still confirms that the separation of the phase angle error into the components in question is valid. For DUT 1, Σ - F is below 2 μs below 30 Hz, and within 0.1 μs for 53 Hz to 3.5 kHz which is well below even the CMC for this frequency range. For DUT 2, Σ - F is within 0.14 μs for the full region for DSWM 1, except at 5 Hz, where the difference is below 0.3 μs.

The standard deviation for each measuring point is within 0.06 μs for DUT 1, 5 Hz to 3.5 kHz. For DUT 2, the standard deviation is within 0.06 μs for 7 Hz to 3.5 kHz. At 5 Hz, the standard deviation is below 0.15 μs. The standard deviation for measurements with DSWM is expected to increase for low frequencies, since fewer cycles are measured.

The phase angle error from the active transformer, i.e. the magnetic circuit and the feed-back circuit, is very close to zero, especially in the AC regime of the zero-flux system; for 25 Hz to 2.2 kHz it ranges from -0.35 μs to -0.22 μs for DUT 1, and for 16 to 600 Hz it ranges from -40 ns to +47 ns for DUT 2.

4.2.2 Frequency normalized phase angle error

Traditionally, the phase angle error, $\Delta\varphi$, is the measurand of interest. However, in the characterization of a zero-flux system described above, it was found that the phase angle error grew linearly with frequency in the AC range. Division of the measured phase angle error with the frequency yielded a nearly constant relationship for frequencies between 20 Hz and 2 kHz, as shown in Figure 10 and Figure 11. The resulting number $\Delta\varphi/f$, is here proposed as a quantity characteristic to the tested equipment, useful when evaluating and comparing the performance of different types of zero-flux systems, together with the frequency range where the constant relationship holds. To the eye, judging when a curve seizes to have a constant value is a lot more obvious than judging when a line seizes to have a constant slope.

The constant error, $\Delta\varphi/f$, is mainly introduced by the read-out buffers, while the active transformers in this region have an error close to zero. In the following sections, two adjustments to the circuitry, one in the read-out buffer and one in the AC loop gain will be attempted and evaluated.

An interesting finding is that although DUT 1 and DUT 2 are of the same type their frequency characteristics are quite different in the low-frequency range. For DUT 1 the phase angle error varies very little in the AC region, and then exhibits a sharp drop at 25 Hz and has a minimum at 12 Hz, whereas DUT 2 has only a small decline towards lower frequencies, but on the other hand the AC region characteristics is less flat than for DUT 1. This would be a natural consequence of a somewhat differing tuning of the feed-back electronics. The minimum of DUT 1 is caused by the active transformer, and most probably by the tuning of the feed-back system.

For increasing frequencies, $\Delta\varphi/f$ seize to be constant, and the point where this happens is the point where the high-frequency range is entered. This region will be further elaborated below.

4.3 Error reduction by construction adjustment

When the origins of the errors have been attributed to different system sections, and the errors have been quantified, a natural next step is to improve the performance of the feed-back circuit and the read-out buffer respectively with respect to these errors.

The first adjustment was to increase the AC feed-back signal amplification, or AC loop gain, by a decrease of the AC feed-back resistance. The second adjustment was to open up the secondary current path on the low-side of the built-in shunt, to introduce an external high performance of the DSWM type shunt resistor as read-out shunt resistor. The adjustments and results will now be described in more detail.

DUT 3 was chosen for the further work, since it allowed an easier access to the different hardware components. DUT 3 was characterized in terms of its scale factor, SF, and its phase angle error, $\Delta\varphi/f$, in the frequency range 10 Hz –100 kHz, referring to its standard input and output signals (SF). Then two adjustments, visualized in Figure 12, were performed. The current was 10 A rms.

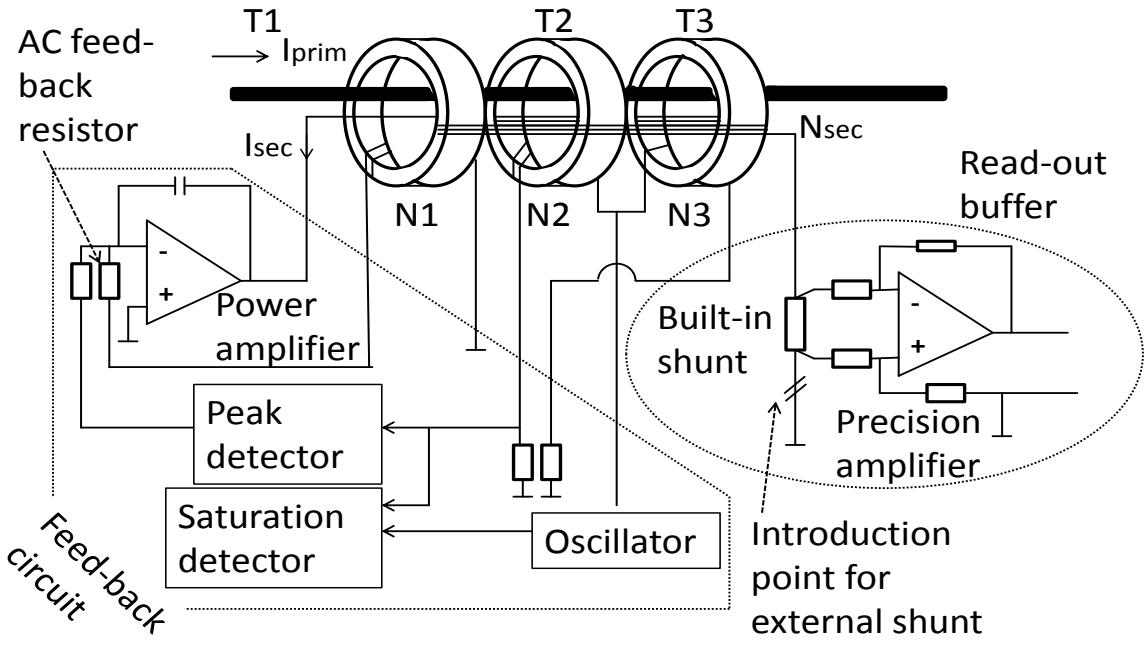

Figure 12: The zero-flux system conceptually divided according to functionality.

4.3.1 Increase of the AC loop gain

During many years of experience at RISE in practical calibration related work, the amplitude frequency dependence of zero-flux systems has been reduced in the DC to 1 kHz span. This has been achieved through increase of the AC loop gain. With this experience as a basis, it was in this work decided to investigate how an adjustment of the AC loop gain would influence the frequency dependence of the amplitude error and the phase angle error, now in the larger frequency range of this work. A variable resistor was hence introduced in parallel with the AC feed-back resistor, thereby lowering the AC feed-back resistance. The scale factor and phase angle error were measured as functions of frequency, in the range 10 Hz to 100 kHz, for a number of different resistance values. The results are presented for the original configuration (denoted as "x1") and for the decrease of the AC loop gain of by a factor 2, 4 and 10, Figure 13 to Figure 16.

In Figure 13 and Figure 14, the scale factor of DUT 3 is presented for the whole measured frequency range, 10 Hz – 100 kHz, and for a zoom-in of the x-axis, 10 Hz – 12 kHz. The solid lines represent the zero-flux system in its original configuration. The scale factor is here presented in absolute units. The current was 10 A rms, and the same throughout the investigation, with the implication that there is no

range dependent error, neither in the zero-flux system, nor in the reference system. Furthermore, the current was only 2 % of the maximum current for the zero-flux system and 10 % of the maximum current of the reference system, from which follows that the error due to heating is negligible. From Figure 13, the most interesting result is that the scale factor varies very much with frequency, almost 45 % from 10 Hz to 100 kHz. The changed AC loop gain improves the high frequency characteristics by some percent, but in this context the improvement is practically irrelevant. This is what would be expected, since the electronics is not operational at these frequencies, and any adjustments there should not yield any dramatic results.

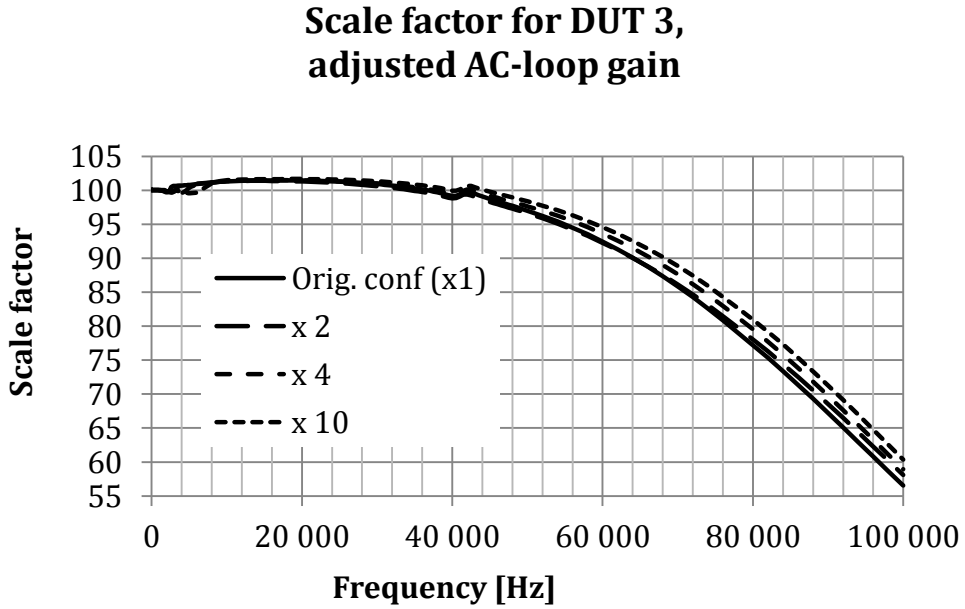

Figure 13: Scale factor for different feed-back signal amplification, 10 Hz – 100 kHz for DUT 3.

A finding of more practical interest can be seen in Figure 14, which is a zoom-in of the frequency range 10 Hz - 12 kHz. The increase of the AC loop gain pushes the transition between the AC region and the high frequency region to higher frequencies. Quantitatively, an increase of the AC resistance value by a factor 10 pushes the upper frequency limit for the normal AC operation of the zero-flux system from circa 1 kHz, corresponding to the 20^{th} harmonic, to circa 3 kHz, corresponding to the 60^{th} harmonic. Hence this adjustment serves to extend the standard operation range. The adjustment however also broadens the transition region, so the optimization for scale factor will be a trade-off depending on application.

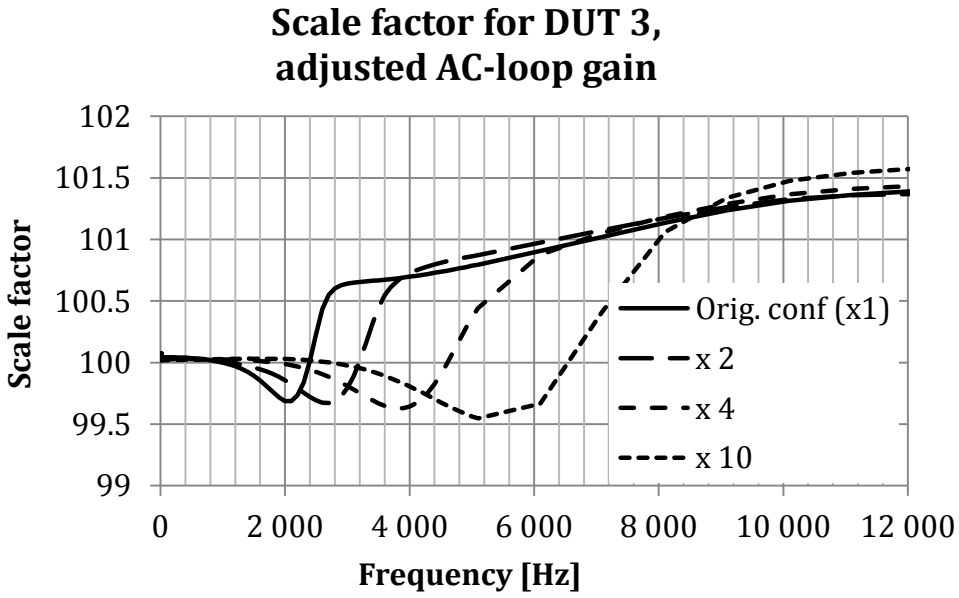

Figure 14: Scale factor for different feed-back signal amplification, 10 Hz – 12 kHz for DUT 3.

If the optimum adjustment for scale factor depends on the application, the effects are more unambiguous for the phase angle error. In Figure 15 and Figure 16, the phase angle error for DUT 3 is presented for the whole measured frequency range, 10 Hz – 100 kHz, and for a zoom-in of the y-axis, to get a clearer picture of the transition region at circa 1 kHz. The solid lines represent the phase angle error of the zero-flux system in its original configuration.

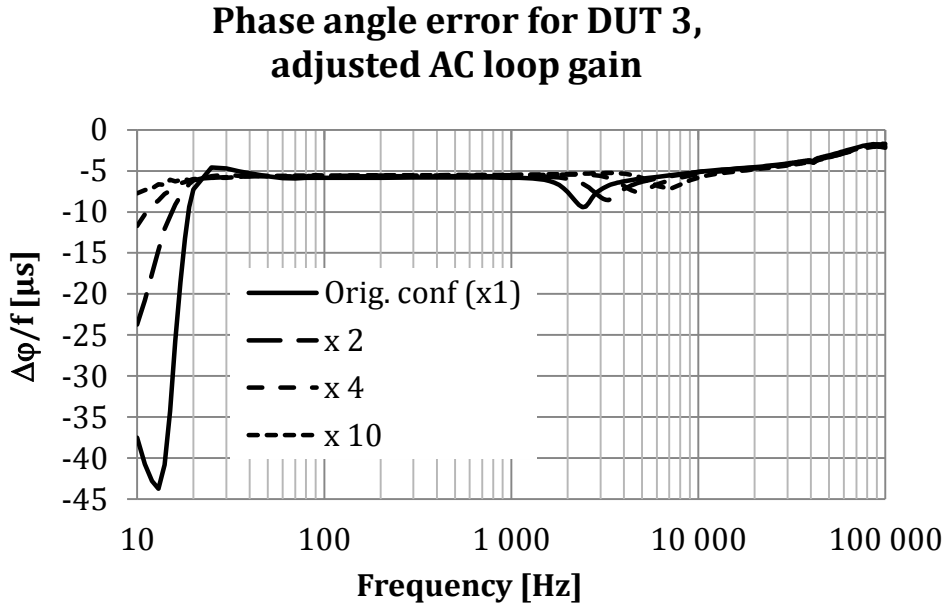

Figure 15: Phase angle error for different feed-back signal amplification, 10 Hz – 100 kHz for DUT 3.

The most obvious result of Figure 15 is that $\Delta\varphi/f$ is drastically reduced in the low frequency region. A further increase of the signal amplification causes a less stable read-out, which would be expected since an increase of the AC loop gain will eventually bring the loop to the point of high frequency oscillations. An increase by a factor 10 is hence optimal for DUT 3, if desired operation is to increase the normal AC operation range in the kHz range. To further push this limit, the operational amplifiers need to be addressed. The design is optimized for DC and AC 50 Hz, and it is assumed that operational amplifiers suppressing higher frequencies are chosen. The optimum AC loop gain must hence be determined for each system and measurement application.

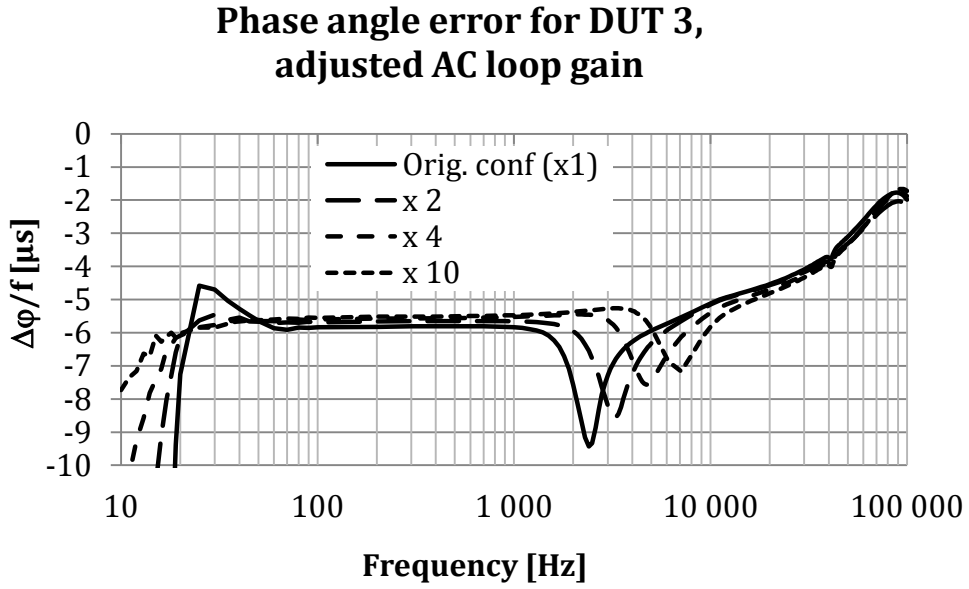

Figure 16: Y-axis zoom of the phase angle error for different feed-back signal amplification for DUT 3, 10 Hz – 100 kHz.

In Figure 16, the same extension of the flat region as in the scale factor case can be seen. The transition region is broadened, and the characteristic is less flat than in the unadjusted case.

In quantitative terms, the AC feed-back adjustment increased the nominal working AC region by flattening the frequency characteristics below 2.4 kHz to within 0.012 % (0.38 % before adjustment) for SF and 2.1 µs (38 µs before adjustment) for $\Delta\varphi/f$. The three frequency regions mentioned in chapter 2 can be clearly seen in Figure 13 to Figure 16, a DC region (below circa 25 Hz), an AC region (circa 25 – circa 1 kHz) and a high frequency region (above circa 1 kHz). The advantages of the AC loop gain adjustment are that the transition between the AC region and the high frequency region is pushed to higher frequencies, enabling zero-flux standard operation measurement up to the 60th harmonic instead of the 20th harmonic, and that the phase angle error dip in the DC region is greatly reduced. The disadvantage is that the transition region is broadened, so if the measuring range of interest includes and exceeds the transition area, the original configuration might prove more useful.

4.3.2 Introduction of an external coaxial shunt resistor

From the measurements of scale factor in the high frequency range, Figure 13, performed at the output terminals of the zero-flux system, it appears that the built-in read-out shunt resistor is more optimized for DC performance than for good high frequency response, which is to be expected for a TopAcc system. This is a logical choice from a design point of view, since the electronic feed-back circuit also has an upper bandwidth of some kHz. Still, it was considered possibly fruitful to characterize and improve the system for considerably higher frequencies, since it would increase the operable range of the device. To improve the frequency response in the high frequency region, an external high precision coaxial shunt resistor designed for frequencies below 1 MHz was introduced in the secondary current path, in series with and on the low-side of the built in shunt resistor in Figure 12. The built in shunt resistor and the external shunt resistor have the nominal DC resistance values of 1 Ω and 0.8 Ω respectively, hence the load in the secondary current path is nearly doubled, but still within the specifications limit of 4 Ω.

An unadjusted DUT 3 type system has typically a SF variation within $50 \cdot 10^{-6}$ and a $\Delta\varphi/f$ variation within 0.15 µs for 50 to 400 Hz. For 50 Hz to 1.5 kHz, the SF variation is well within 0.2 % and the $\Delta\varphi/f$ variation within 0.5 µs. Outside this frequency range, the SF error increases as can be seen from the solid lines in Figure 13 and Figure 14.

A comparison of the output signal levels from the built-in shunt with and without the external shunt present was performed. The difference for SF was 1.7 %, 10 Hz – 100 kHz and within 0.4 % below 50 kHz. $\Delta\varphi/f$ was within 8 %, 35 Hz – 100 kHz. This is at first sight large numbers but deemed acceptable, since the experiment still fills it purpose; namely to show that the frequency response is greatly improved. For frequencies below 35 Hz, $\Delta\varphi/f$ for the built-in shunt was between 14 % and 67 %

closer to zero with the increased burden present, as compared to the original burden. This suggests that the increased burden in the secondary current path serves to lower the phase angle error.

In Figure 17 to Figure 19, the scale factor of DUT 3 is presented for the whole frequency range and for some different zoom-ins of the x- and y-axes. The solid and the dashed lines represent the SF measured utilizing the built-in and the external shunt, at the same burden in the secondary circuit, that is, both shunts are present in the circuit and only the read-out terminals are different. The dotted lines represent measurements where a short circuit was applied between the input terminals of the built-in shunt.

Figure 17 mainly shows that for very high frequencies, above some 20 kHz, the frequency dependence of the built-in shunt causes major errors, as is expected for a DC or low-frequency AC shunt. The changed burden in the secondary circuit given by the short-circuiting of the built-in shunt shows no effect on this large scale.

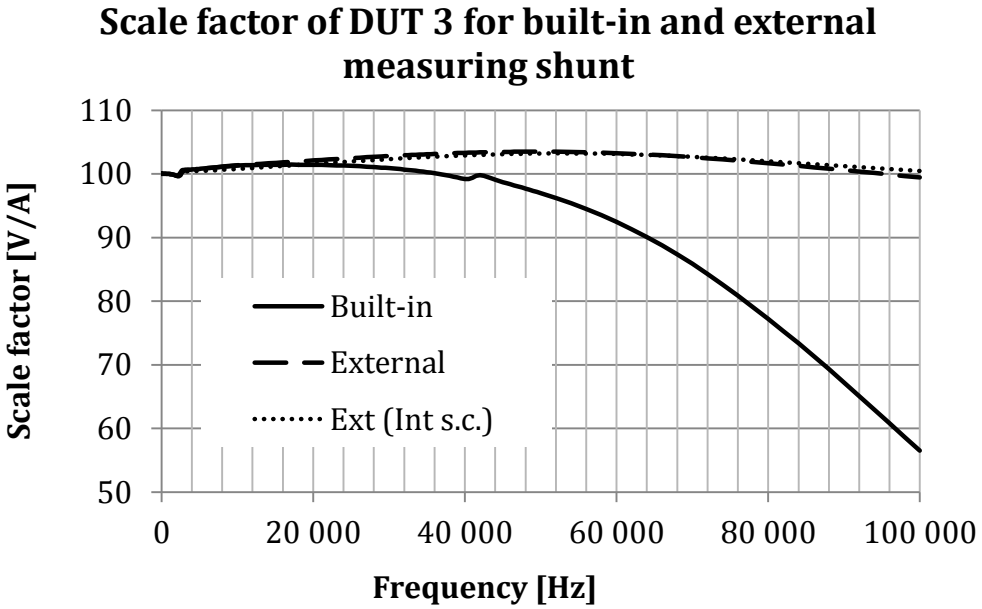

Figure 17: Scale factor, SF, for 10 Hz to 100 kHz for DUT 3 for the built-in shunt and the external shunt.

Figure 18 shows that given the same burden in the secondary circuit, the built-in shunt and the external one shows the same behaviour to some 8 kHz, which is impressive results for the built-in shunt.

The built-in shunt is even, in a sense, better than the external, AC-optimized one for frequencies below 40 kHz, its characteristics stays within 2.5 % in this region, whereas the external shunt varies close to 4 %. At 40 kHz, the built-in shunt exhibits a knee, and at even higher frequencies, its characteristics drops rapidly. The knee seen in this curve cannot be seen for the external shunt, and it is expected, if not confirmed, that this knee is caused by the precision amplifier in the read-out buffer.

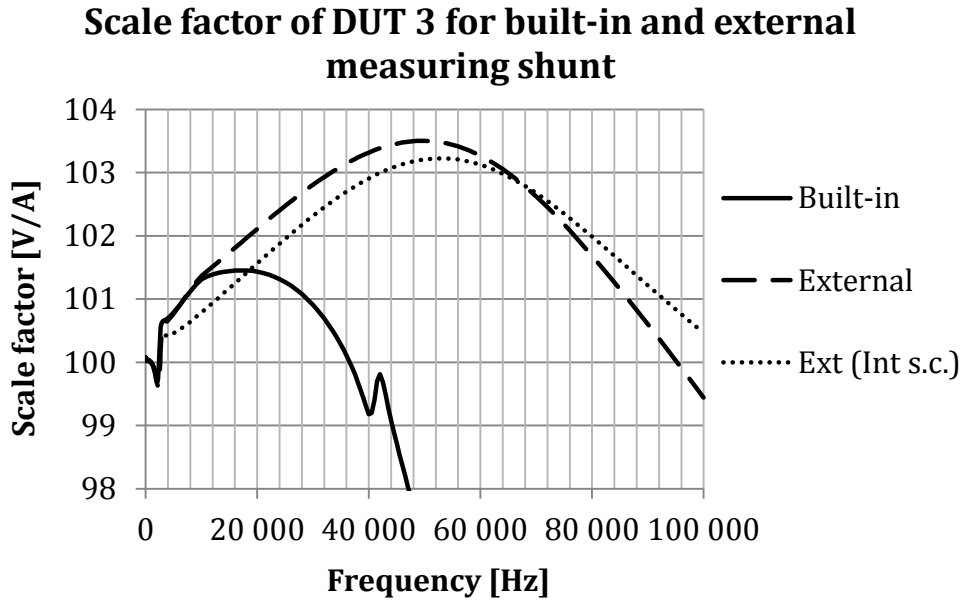

Figure 18: Zoom-in of the scale factor, SF for 10 Hz to 100 kHz for DUT 3 for the built-in shunt and the external shunt.

In Figure 19 the scale factor for the system in normal operation, or in its AC region, and the transition to the high frequency region is shown. As expected, no useful improvements are seen, since the built-in shunt is optimized for this region. The dotted line, where the built-in shunt has been short-circuited, shows that the burden chosen (1 Ω for the built in shunt) is a better choice than the 1.8 Ω, which is the resulting burden with both shunts in the secondary circuit.

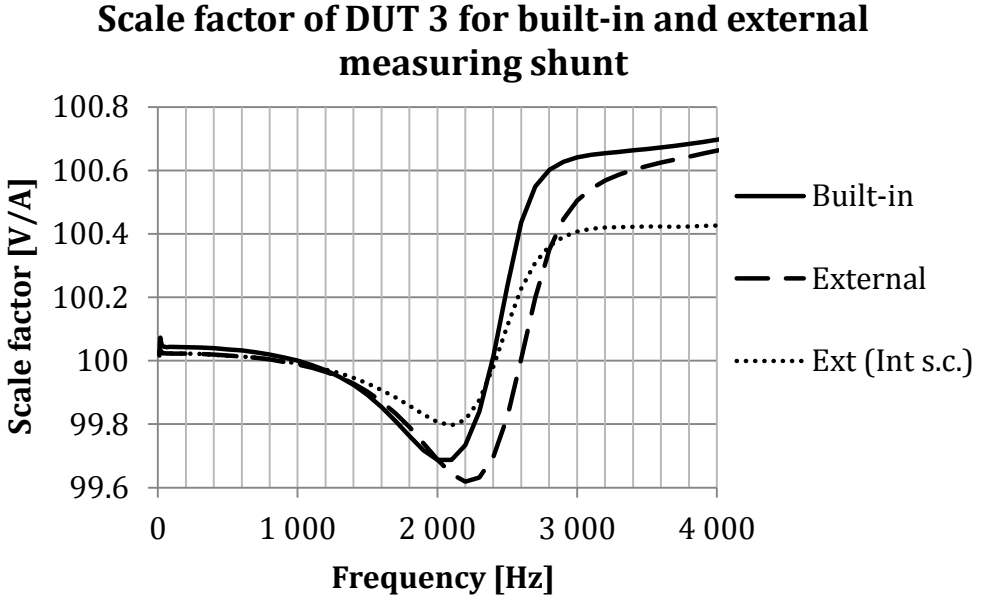

Figure 19: Zoom-in of the scale factor, SF for the DC- and the AC regions, 10 Hz to 4 kHz, for DUT 3 for the built-in shunt and the external shunt.

Figure 20 and Figure 21, show the phase angle error divided by frequency of DUT 3, for the whole frequency range and for a y-axis zoom-in of the AC region and the high-frequency region. The solid and the dashed lines represent $\Delta\varphi/f$ measured with the built-in and the external shunt, at the same burden in the secondary circuit, that is, both shunts are present in the circuit and only the read-out

terminals are different. The dotted lines represent measurements where a short circuit was applied between the input terminals of the built-in shunt.

What is interesting here is that the introduction of an AC current shunt practically removes the constant $\Delta\varphi/f$ error in the AC region, and reduces it in the DC and the high-frequency regions. Instead of a constant $\Delta\varphi/f$ error of about -6 µs, the error is reduced to less than 0.1 µs. The importance of this result depends on the application and the measurement uncertainty needed. It is also well in line with what is generally expected; a shunt optimized for AC will not introduce any dramatic phase shift, whereas a DC or low AC shunt may very well do so.

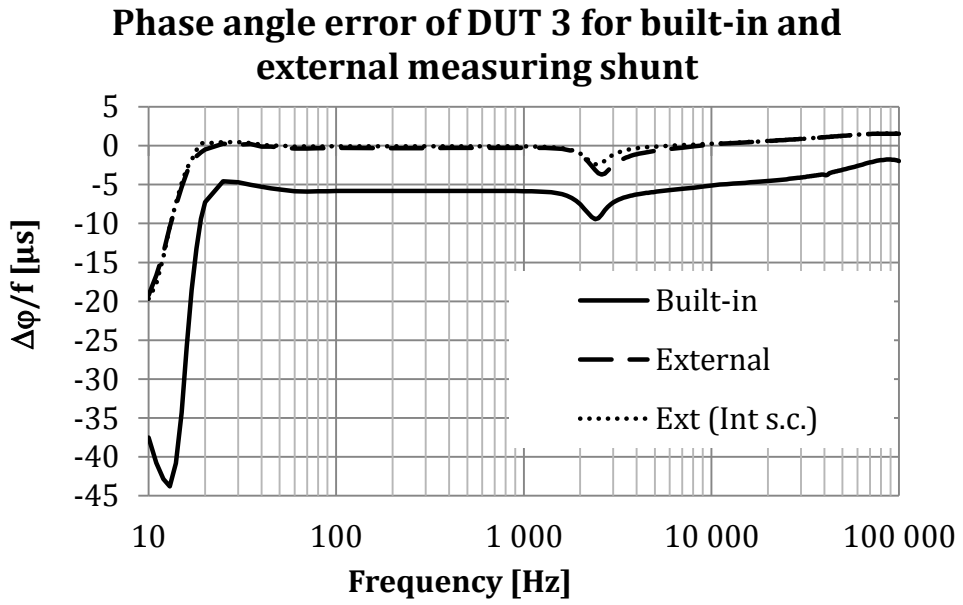

Figure 20: $\Delta\varphi/f$ for DUT 3, 10 Hz to 100 kHz, for the built-in shunt and the external shunt.

Figure 21 is a y-axis zoom-in of Figure 20 i.e. without the low frequency characteristics. In this resolution it can be seen that there is a small secondary circuit burden dependence (dotted versus dashed line) , which is to be expected since the maximum specified burden is 4 Ω, the built-in shunt has a resistance value of 1 Ω and the external shunt 0.8 Ω.

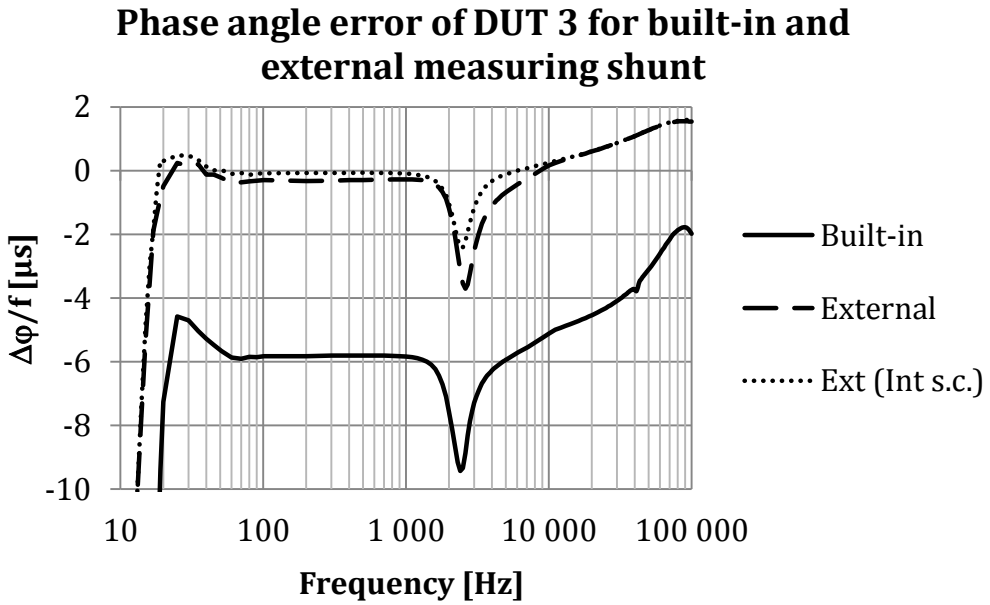

Figure 21: Y-axis zoom-in of $\Delta\varphi/f$ for DUT 3, 10 Hz to 100 kHz, for the built-in shunt and the external shunt.

Figure 22 and Figure 23 introduce nothing already shown, but conclude the SF and *Δφ/f* characteristics for the whole investigated frequency range, for DUT 3 in its original configuration (solid line) and with the two optimizations regarding AC loop gain and read-out shunt resistor (dashed line).

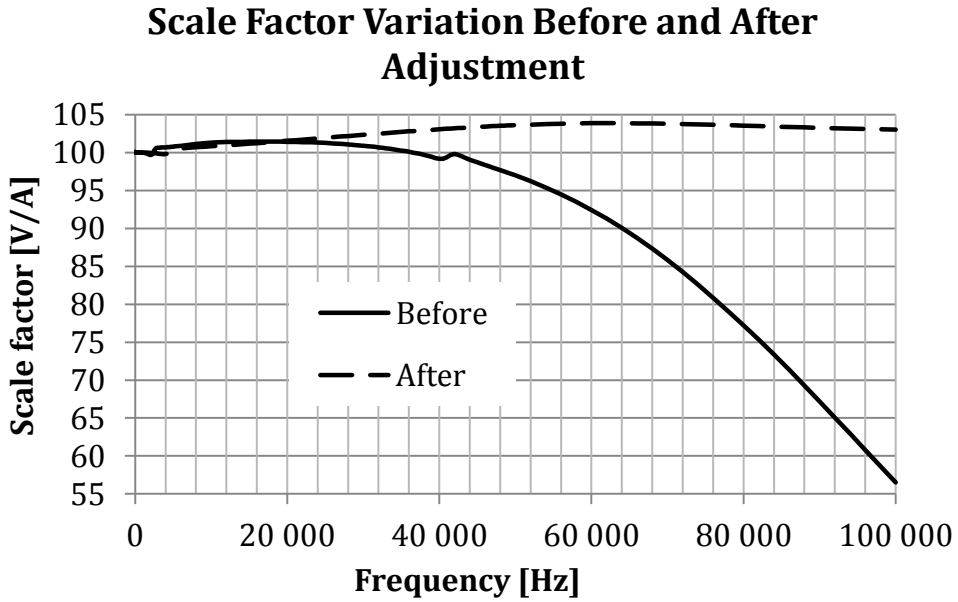

Figure 22: Scale factor, SF for 10 Hz to 100 kHz for DUT 3 before adjustment, and after introduction of external shunt and increased amplification in the feed-back circuit by a factor 4, which was deemed optimal to reduce errors.

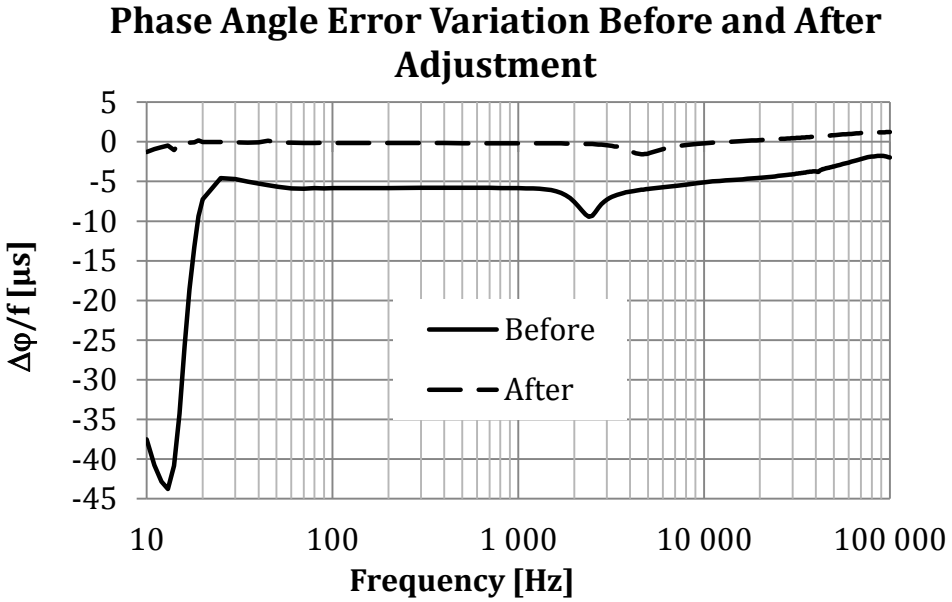

Figure 23: *Δφ/f* for 10 Hz to 100 kHz for DUT 3 before adjustment, and after introduction of external shunt and increased amplification in the feed-back circuit by a factor 4, which was deemed optimal to reduce errors.

To summarize the findings of this section, the adjustment of the AC loop gain pushed the transition between the AC and the high frequency region to enable measurements of 60th harmonic instead of just 20th harmonic, but also broadened the transition region. Which value is optimal depends heavily on the application. If a flat frequency response in the low frequency range (10 – 40 Hz) is desirable, increase of the AC loop gain by a factor 10 greatly reduce the phase angle error. If a maximum normal AC operations range (up to 3 kHz) is desirable, the aforementioned adjustment of AC loop gain is also optimal. Since this adjustment also broadens the transition area and increases the risk of loop instability, the AC loop gain is however better left as it is, if also higher frequencies (3 - 100 kHz) are of interest. The introduction of an AC shunt resistor as read-out resistor reduced the phase angle error in the whole frequency spectrum and from 5.5 µs to almost zero in the AC region. It also reduced the high frequency SF error quite dramatically, from 45 % for the built-in shunt to 3.5 %, but below 1 kHz no improvement could be detected. The built-in shunt resistor works reasonably well below 9 kHz – SF results coincide within 0.08 % as compared to the external one. A quick summary of the most important numbers are given in Table V.

Table V. A short summary of the error reductions for scale factor and *Δφ/f* for adjusted AC-loop gain and introduction of an AC read-out shunt resistor.

		Scale factor		*Δφ/f*	
	Frequency	Unadjusted system	Adjusted system	Unadjusted system	Adjusted system
AC-loop gain	10 Hz - 2.4 kHz	0.38 %	0.12 %	38 µs	2.1 µs
AC read-out shunt	50 - 400 Hz	$50 \cdot 10^{-6}$		0.15 µs	
	50 – 1500 Hz	0.2 %		0.5 µs	

4.4 Comparison between two reference systems

To reach the higher frequencies of this investigation, DSWM 2 was employed as reference system. DSWM 1 has a specified working range of 10 Hz – 1 kHz, and a maximum technical upper frequency limit of 3.5 kHz. DSWM 2 is specified for frequencies between 1 kHz and 1 MHz, and the upper frequency limit is well above the frequency range of interest in this work. Technically, DSWM 2 performs measurements down to 10 Hz, and it is in this overlapping, technically possible but not necessarily optimal, working frequency range of 10 Hz – 3.5 kHz that a comparison between the two systems is performed.

A comparison of DSWM 1 and DSWM 2 with respect to SF and *Δφ/f*, utilizing DUT 1 was performed. However, any of the three DUTs could have been used for this measurement, since the DUT acts here only as a transfer standard.

In Figure 24 to Figure 26 the results from this comparison are given. In Figure 24, *Δφ/f* of the full system is shown for DUT 1. Except for the 10 Hz point, the difference between the two systems is within 0.4 µs.

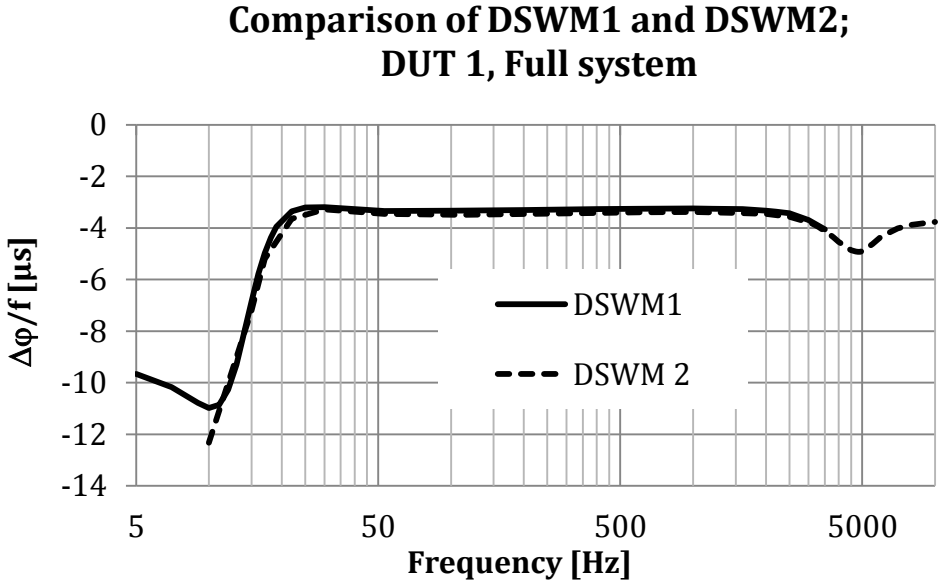

Figure 24: Phase angle error of DUT 1, full system, with DSWM 1 and DSWM 2.

In Figure 25, the phase angle error of the active transformer is shown for DUT 1. The difference between the two DSWM systems is largest for this measurement; within 1.6 µs and only weakly frequency dependent.

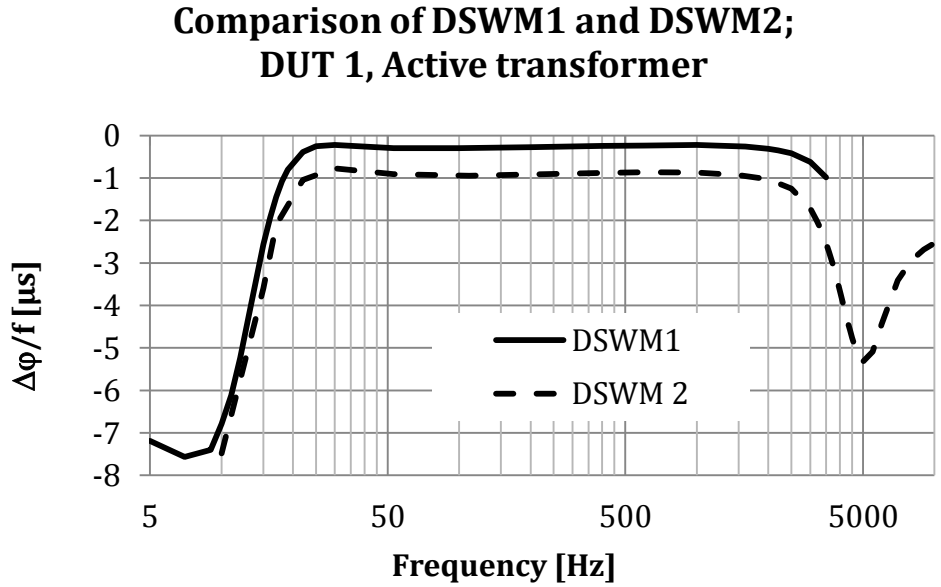

Figure 25: Phase angle error of DUT 1, measuring head, with DSWM 1 and DSWM 2.

In Figure 26, the phase angle error of the electronic unit is shown for DUT 1.

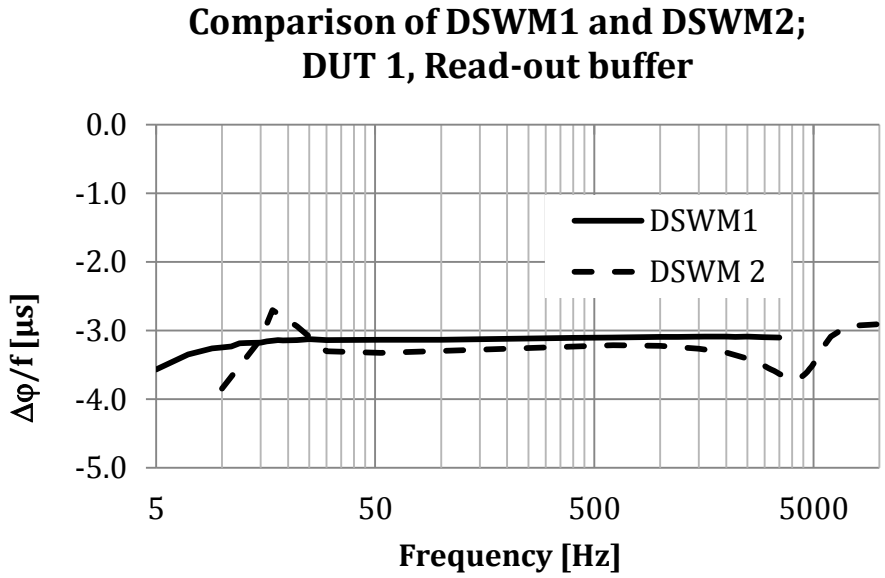

Figure 26: Phase angle error of DUT 1, electronic unit, with DSWM 1 and DSWM 2.

The difference between the two systems for the read-out buffer is never greater than 0.6 µs in magnitude, but this measurement shows the most irregular behaviour between the two reference systems. Measurements from DSWM 1 form a smooth curve, while DSWM 2 indicates phase transitions which are not detected with DSWM 1.

The differences between measurements performed with the two DSWM systems are larger than the minimum measurement uncertainties for the DSWM systems (CMCs), which can be expected, since the comparison frequencies are always outside the ideal range for one of the systems. For the full system, the results of this comparison are best, because the errors of the read-out buffer and of the active transformer partly cancel each other. Had the goal with this work been the formally correct comparison to ensure traceability and agreement between two reference systems, our work would just have started here. The first step would have been to find the exact cause of the deviations, perform a complete measurement uncertainty budget for all the components in the measurement setup, including type A and type B uncertainties. However, in this application, a qualitative agreement is deemed good enough.

4.5 Origin, quantification and reduction of errors

The phase angle error of a zero-flux current measuring system was found to be constant in time units in the frequency range of about 20 Hz to 2.5 kHz, and is hence possible to compensate for. The frequency normalized phase angle error $\Delta\varphi/f$, is proposed as a quantity characteristic to and useful for the evaluation of and comparison between different types of zero-flux systems. At about 5 Hz to 20 Hz, a transition between the DC and AC regions was identified. At about 2.5 kHz, $\Delta\varphi/f$ seized to be constant, and the high-frequency region is entered.

The constant error, $\Delta\varphi/f$, is mainly introduced by the read-out buffers, while the active transformers in this region have an error close to zero.

The difference between the measured errors of the full system and the summed contributions from the different parts of the system is small compared to, or at worst of the same magnitude as, the measurement uncertainty of the reference system. The conceptual sectioning of the zero-flux system of section 4.1 was shown valid and useful as a model in the efforts to improve the high-frequency characteristics of a zero-flux system.

During many years of experience at RISE in practical calibration related work, the amplitude frequency dependence of zero-flux systems has been improved in the DC to 1 kHz span by adjustment

of the AC loop gain. With this procedure adapted in this work for the frequency span 10 Hz – 100 kHz it was shown that the adjustment of the AC loop gain serves to extend the normal AC operation range also above 1 kHz. Quantitatively, an increase of the AC resistance value by a factor 10 pushed the upper frequency limit from circa 1 kHz, corresponding to the 20^{th} harmonic, to circa 3 kHz, corresponding to the 60^{th} harmonic. However, the adjustment also broadened the transition region between the AC operation region and the high-frequency region, and increased the risk of loop instability. The optimization will hence be a trade-off depending on application. There are also indications that a somewhat increased burden in the secondary current path serves to lower the phase angle error.

The introduction of an AC shunt resistor as read-out resistor reduced the phase angle error in the whole frequency span, and to almost zero in the AC region. It also reduced the high frequency SF error quite dramatically, from 45 % for the built-in shunt to 3.5 %. The built-in shunt resistor works reasonably well below 9 kHz – SF results coincide within 0.08 % as compared to the external one.

The agreement between measurements on the same DUT but with different reference systems was fair enough for the qualitative assessment of whether a certain adjustment to the circuitry has a positive effect or not.

5 The geometry of the primary current loop

IN chapter 4, it was shown that it is possible to improve the high frequency characteristics of a zero-flux current measuring system by replacing the built-in read-out resistor with a high precision coaxial shunt resistor and by increasing the AC loop gain. The frequency characteristics are however also affected by the total measurement setup. In this chapter effects of different setup aspects will be elaborated.

It does not take much practical experience of measurements with non-contact measuring techniques, to realize that the geometry of the primary current loop, as well as the positioning of the current sensor around the current conductor, is of great importance for accurate measurements. In an ideal measurement setup, the sensor should be mounted in such a way that it senses only the homogenous and undisturbed magnetic field from the current to be measured. This means that it should ideally be placed absolutely symmetrically around the current conductor, infinitely far away from the current source, the return conductor(s), and from any other current carrying conductors or time-varying fields.

In practice, these conditions are not achievable. Instead practical considerations to avoid effects of inhomogeneities and disturbing magnetic fields must be made. To obtain a core design immune to disturbances, the core needs sufficient cross-section and permeability to avoid local saturation. Magnetic screening material can be applied to the outer circumference and the sides of the core to minimize the influences from disturbing magnetic fields. The user must also have a good grasp of the measurement error and measurement uncertainty related to the measurement setup. Uncertainty components due to non-ideal geometrical conditions must be considered as they are shown to be more pronounced at high frequencies.

This chapter is dedicated to a thorough investigation of how the geometry of the primary current loop and the positioning of the sensor in the resulting magnetic field affect the measured SF and $\Delta\varphi/f$ for this equipment. Thereby a technique for the investigation of the effects of geometry within mounting is demonstrated. This technique is generally applicable for all non-contact measurement systems. In this chapter scale factor measured at different frequencies is presented per unit, relative to 53 Hz, and is calculated as

$$SF = \frac{Measured\ ratio}{Measured\ ratio\ at\ 53\ Hz}$$

unless otherwise stated. This relative scale factor can also be considered as scale factor sensitivity. In this chapter, mainly the scale factor was considered. Phase angle error is briefly mentioned in Chapter 5.7.

To investigate the sensitivity of the magnetic circuit to its orientation in the magnetic field, DUT 4 as defined in section 3.5, was utilized in the next sets of measurements. To deduce the influences from the positioning on the measurement error, five basic geometrical quantities, described in Figure 27 and Figure 28, are considered; (i) the de-centring of the primary conductor through the sensor, (ii) the distance from the sensor to the return conductor, (iii) the distance from the sensor to the radially oriented part of the primary conductor, (iv) the tilt of the primary current conductor and (v) the rotation of the sensor, i. e. the relative position of the internal measurement and zero-flux control cable connection point, hereafter referred to as the cable connection point.

(i): De-centring is a well-known error source for any measurement technician. The problem is usually handled either by taking the uttermost care preparing the setup and/or through measurement of some different de-centring positions and accountancy for the introduced measurement error. It should be pointed out that de-centring in the x-direction and the y-direction are different since the cable connection point represents an asymmetry. Moreover a second asymmetry in the x-direction is caused by the return conductor.

(ii): The radially oriented part of the return conductor generates a magnetic field unable to induce a rotational magnetic field in the core and should hence not affect the measurement. However, any current carrying conductor placed close to the sensor gives rise to a magnetic field gradient, which can cause local saturation, equivalent to higher magnetic reluctance and loss of measurement accuracy. On the other hand it is possible to shield the sensor against these magnetic components, which is also done

in the cores utilized in this project. Without shielding μ-metal, the effects are expected to be more pronounced.

(iii): The part of the return conductor being parallel to the current to be measured generates a magnetic field in the same plane as the one to be measured. To balance the influence of this component, it is common practice to split the return conductor in two, thereby achieving a symmetrical current loop, where the magnetic field from the return conductor on one side will be counteracted by the magnetic field from the return conductor on the other side. The magnetic fields from the two return conductors will cancel each other on the symmetry line. However, this canceling is not valid in the magnetic core, its mass being distributed around the symmetry line. Hence, this practice was not chosen here. Another reason not to split the return conductor in two was that the larger enclosed area of the primary current loop increases the load inductance for the current source, reducing the maximum available frequency at a given current level. Since the effects accounted for in this work are more pronounced at higher frequencies, the choice of only one return conductor was made to point out the effect as such.

(iv): When the current conductor is tilted as compared to the sensor orientation, the magnetic field can be decomposed into one component in the direction to be detected by the sensor, and one orthogonal component. Usually, the tilt angle α is small, since the centre hole of the sensor is not larger than necessary. Furthermore, tilt is probably the easiest geometrical condition to avoid, unless the measurement setup is very tight. Hence, this error is not expected to be large, but was anyway investigated for the completeness of the analysis.

(v): Rotation of the sensor introduces two unknown factors; the effect of the magnetic field on the measurement and zero-flux control cable itself, and the effects on the point where the cable is physically attached to the sensor. The cable is a screened twisted-pair cable chosen to be immune to external stray fields. The screening counteracts effects from electrical fields and the twisting removes differential mode (DM) induced voltages. Effects from the common-mode (CM) induced voltage can be avoided by measuring floating potential difference between the two leads. Furthermore, the internal connection of the cable to the windings of the transformer necessitates the removal of screening and untwisting of the leads. This may lead to additional errors. However, the details of the cable and its connection to the windings are not investigated in detail in this work.

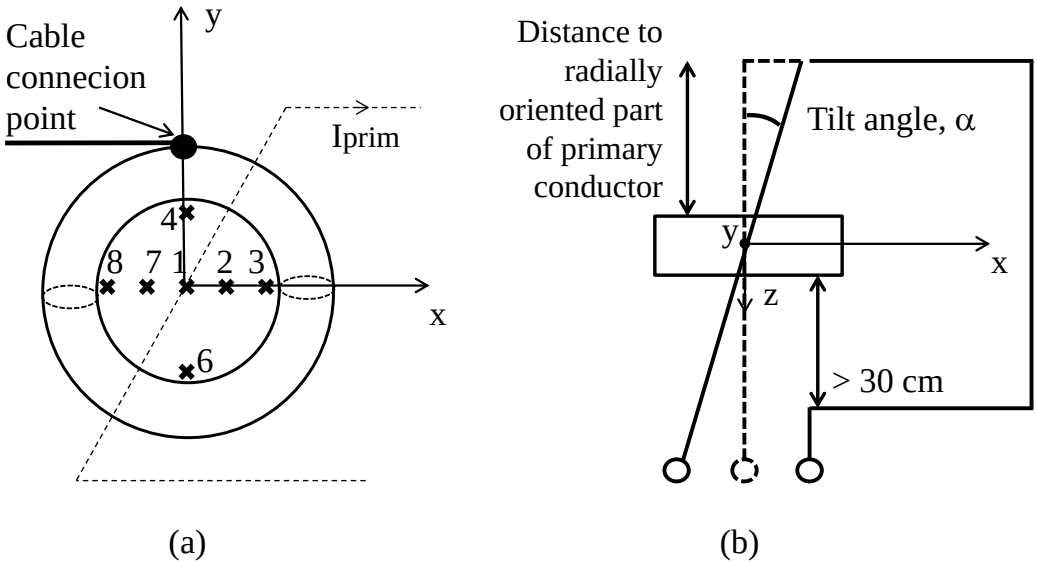

Figure 27: (a) Definition of the positions of the primary conductor for investigation of de-centering. The inner diameter of the hole through the core is 3.5 cm and the diameter of the primary conductor was 10 mm. **(b)** Definitions of the distance to the radially oriented part of the primary conductor and the tilt angle, α. The y-axis is directed out of the paper.

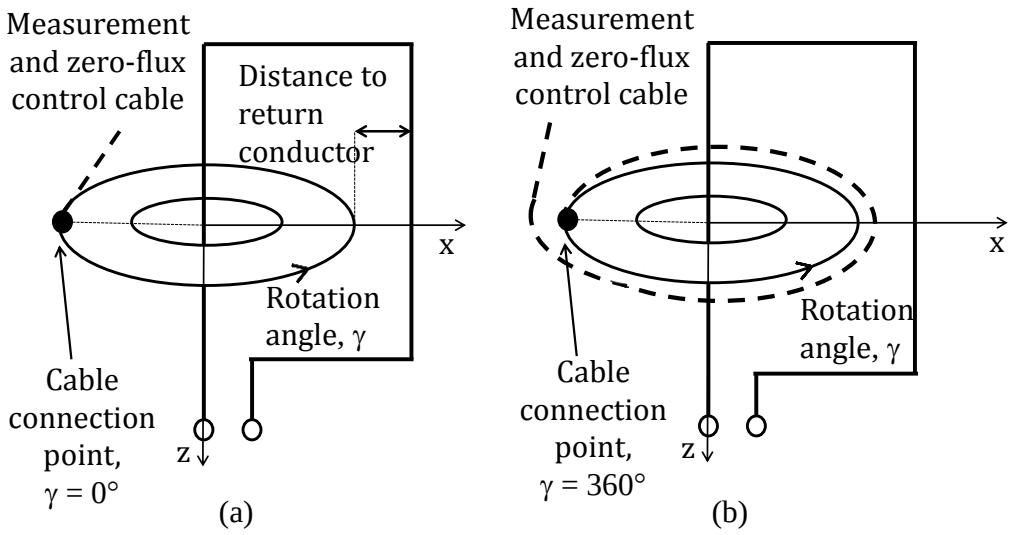

Figure 28: (a) Definition of rotation angle, γ, and the distance to the return conductor. **(b)** Rotation of the sensor means that an increasing portion of the cable will be inside the primary current loop, as the cable connection point's position is shifted between outside the primary current loop (γ = 0° and 360° respectively) and inside the loop (γ = 180° and 540° respectively).

In the measurements presented below, the primary current conductor was centred, the distance to the radially oriented part of the primary conductor and the distance to the return conductor were at least 30 cm, the rotation angle was 90° and the tilt angle was 0°, unless otherwise stated. The current dependence of the SF was measured to be below $10 \cdot 10^{-6}$ in the range I = 3 – 12 A (peak value, sinusoidal) and f = 10 Hz – 25 kHz. The primary conductor was a copper rod with a diameter of 10 mm. A 12 A sinusoidal current with the frequency range 10 Hz – 25 kHz was used. The presented results are normalized to 53 Hz.

5.1 De-centring

The scale factor was measured for the positions defined in Figure 27a. The obtained scale factor frequency dependence is presented in Figure 29 and Figure 30.

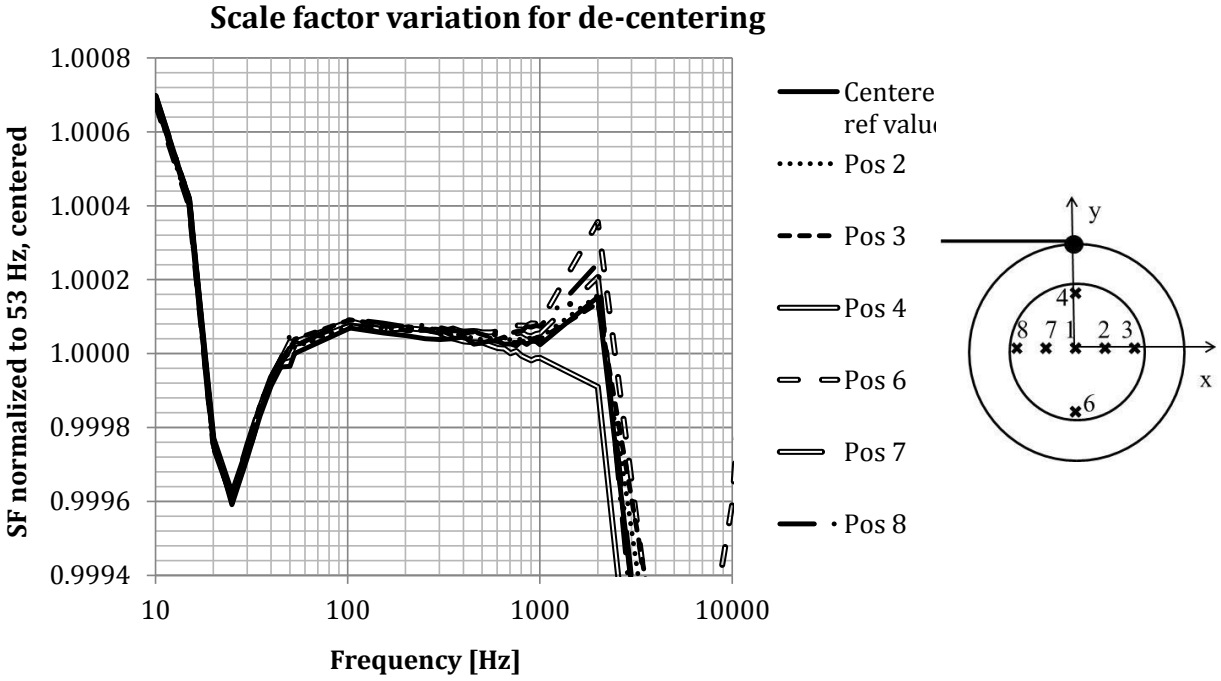

Figure 29: Left: Normalized SF as a function of frequency, 10 Hz – 10 kHz, for different de-centring positions. **Right:** Positions of primary conductor, Fig. 27a repeated.

The effects of de-centring are small below circa 1 kHz – the curves show small deviations from each other even at this scale. At 50 Hz a larger deviation can be seen, most likely caused by ambient 50 Hz noise, and for this reason, 53 Hz values are generally reported in this project. Around 1 kHz, the same transition region between the active AC compensation mode and the passive AC mode as in for example Figure 14 can be seen (also discussed in section 2.3). In the passive AC mode however, de-centring causes the large SF changes also seen in Figure 30.

In Figure 30 the SF effects of de-centring are again shown, now with a focus on high frequencies.

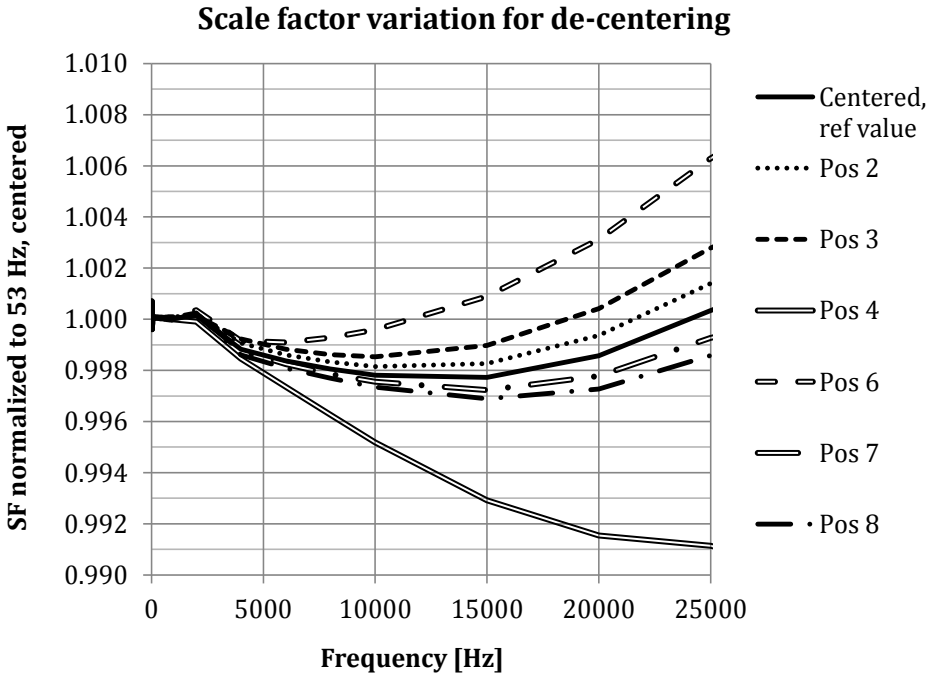

Figure 30: Normalized SF as a function of frequency for different de-centring positions.

The solid line and the four curves closest to it show de-centring in the x-direction (positions 8, 7, 1, 2, 3). The two outermost curves show de-centring in the y-direction (positions 4, 1, 6). As can be seen, de-centring in the x-direction causes less effect than de-centring in the y-direction, even when the distance to the centre is the same.

In points 2 and 7 or 3 and 8, the distances to the centre are the same, but de-centring bringing the cable connection point further away from the return conductor (positions 2 and 3) increases the SF while de-centring bringing the cable connection point closer to the return conductor (positions 7 and 8) decreases the SF.

For de-centring in the y-direction, position 6 increases the SF and position 4 decreases the SF. The change in scale factor when moving the primary conductor from position 1 to position 4 is circa twice as large as compared to moving the primary conductor from position 1 to position 6.

The above mentioned (Section 5.1(v)) immunity deficiency to stray fields where the cable is untwisted and attached to the core winding is a possible reason to the seen effects on SF. Another possible cause to the observation is the changed electromagnetic environment of the cable connection point.

The results above will now be further elaborated on by examination of the SF dependence on distance to the centre for some chosen frequencies. In Figure 31 and Figure 32, the SF is shown as a function of the distance from the core centre for 25 kHz and 10 kHz. The measured SF value is normalized, at each frequency, to the SF value obtained with centred current conductor. The only parameter affecting the SF is hence the distance to the core centre.

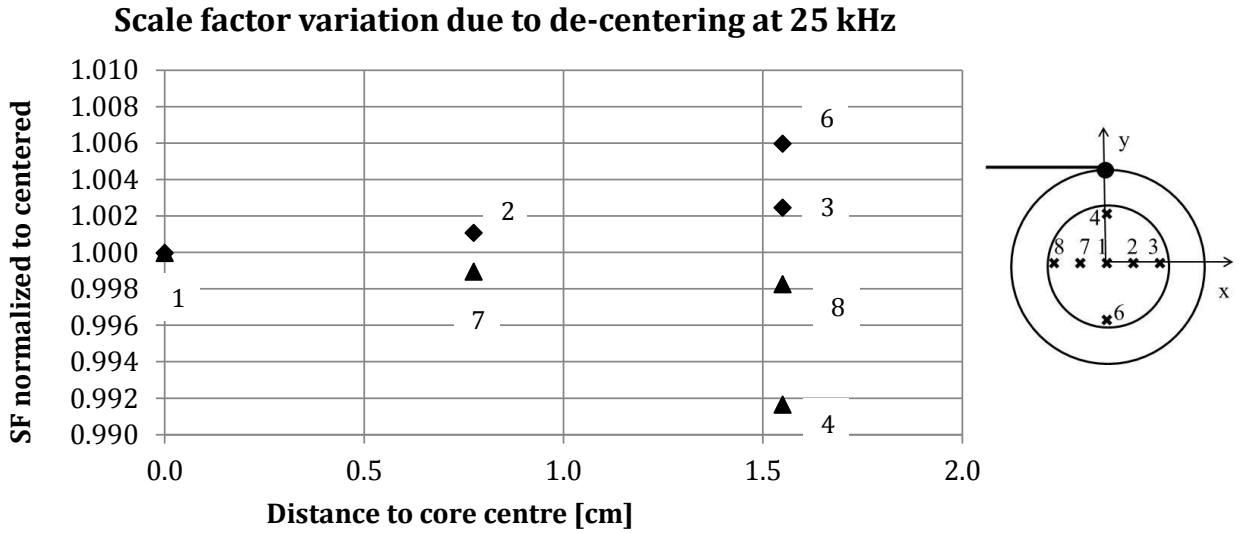

Figure 31: Left: Normalized SF for the different de-centring positions at 25 kHz. The x-axis is here the geometrical distance of the current conductor to the geometrical centre of the core. **Right:** Positions of primary conductor (Figure 27a repeated).

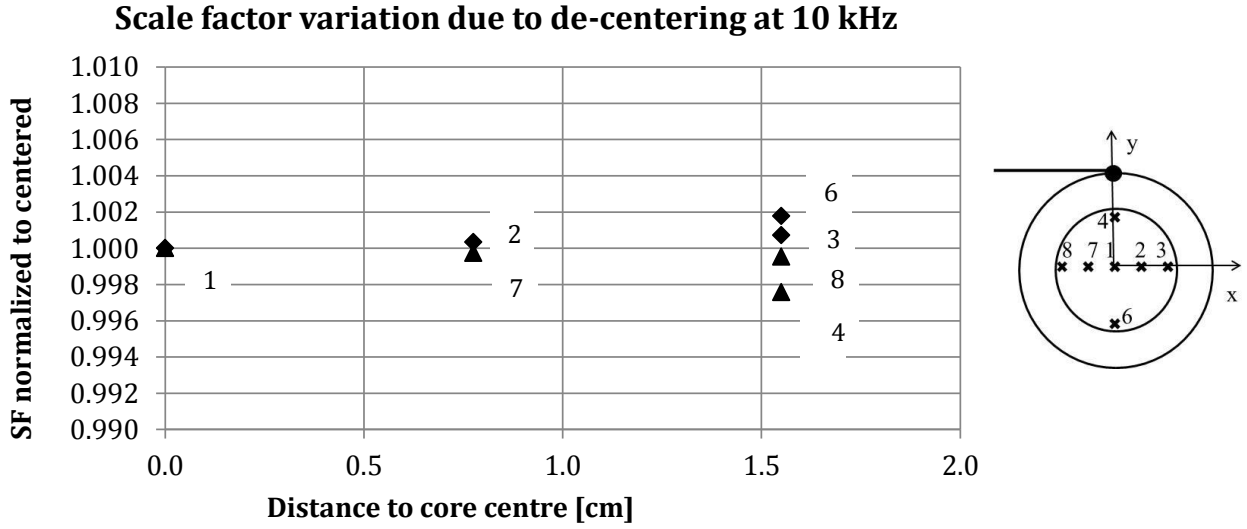

Figure 32: Normalized SF for the different de-centring positions at 10 kHz. The x-axis is here the geometrical distance of the current conductor to the geometrical centre of the core.

Two effects other than the frequency dependence can be seen:

1. For the geometrically seemingly equal points when it comes to the magnetic core and the windings; 3, 4, 6 and 8 (the current conductor is pressed against the inner circumference of the core), the SF deviations are different from each other, suggesting that the asymmetry introduced by the cable connection point has an effect that has to be accounted for.
2. Taking the cable connection point between cable and winding into account, the points which have the same distance to this point (2 and 7) and (3 and 8) respectively show different SF variation; the deviations have roughly the same amplitude, but opposing signs. This suggests that the magnetic environment around the measurement and zero-flux control cable connection point is not only influenced by the primary conductor, but the entire current loop. Further, there might also be an influence from the magnetic environment around this cable.

From the results in Figure 31 and Figure 32, it is possible that the distance to the cable connection point is more important than the distance to the central point. In Figure 33 and Figure 34, SF is shown as a function of the distance from the cable connection point for 25 kHz and 10 kHz. The measured SF value is normalized, at each frequency, to the SF value obtained with centred current conductor. The only parameter affecting the SF is hence the distance from the cable connection point.

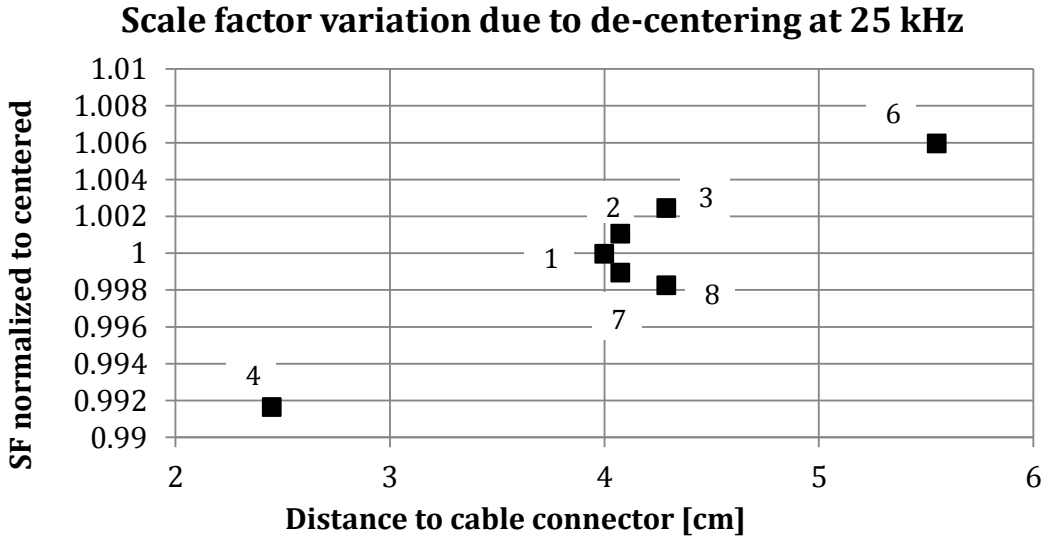

Figure 33: Normalized SF for the different de-centring positions at 25 kHz. The x-axis is here the geometrical distance of the current conductor to the cable connection point.

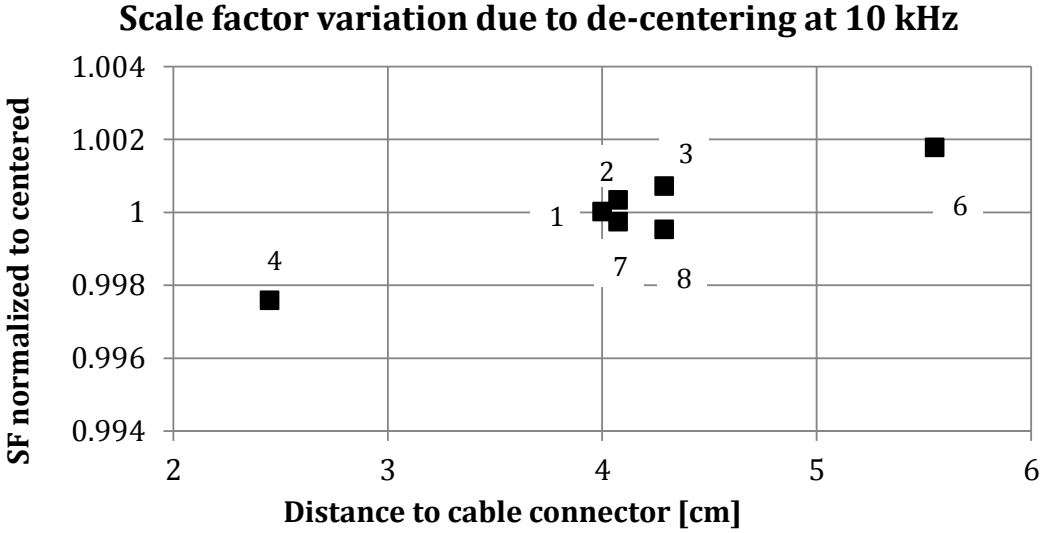

Figure 34: Normalized SF for the different de-centring positions at 10 kHz. The x-axis is here the geometrical distance of the current conductor to the cable connection point.

From Figure 33 and Figure 34, no firm conclusions can be drawn on a plausible mathematical model to describe the SF dependence on distance from the cable connection point. The SF change due to de-centring is strongly frequency dependent, most clearly seen in Figure 30. For 53 Hz, the maximum SF change is 0.0039 %, for 1 kHz 0.096 % and for 25 kHz 1.5 %. Hence, the results show that the SF changes are comparably small in the AC compensation mode, while they increase rapidly in the passive AC mode, and furthermore depend heavily on in which direction the de-centring is done.

The larger de-centring dependence at high frequencies coincides with the transition from the active

AC compensation mode to the passive AC mode. Further, one can suspect that the details of the connection between the measurement and zero-flux control cable and the core windings also affect the results. The reason(s) to these two observed phenomena are not known. These reasons are however not central to this thesis and are not further discussed.

The practical implications of this section are:

(1) Centring of the core around the primary conductor may be the dominant contribution to uncertainty for frequencies above a couple of kHz.

(2) In the active AC compensation mode, the effects of de-centring are small compared to the effects in the passive AC mode, with transition at circa 1 kHz. As a matter of fact, the results show that reasonable corrections due to de-centring can be achieved below the transition frequency.

(3) Positioning of the cable connection point relative to the primary current conductor needs to be considered and included in a measurement uncertainty calculation.

(4) The distance to the cable connection point seems to have a greater impact than the de-centring at high frequencies.

Altogether, the results of this section show that the influence of de-centring cannot be neglected. It is however possible to setup an uncertainty budget that takes into account a reasonable, easily achievable, requirement on de-centring, which can be used to develop a corresponding uncertainty contribution.

5.2 Distance to radially oriented part of primary conductor

The scale factor was measured for variation of the radial distance to the primary conductor as defined in Figure 28a. In Figure 35, the normalized SF as a function of frequency for different distances to the radially oriented part of the primary conductor is shown. The results are normalized to the SF at a distance of 30 cm, 53 Hz.

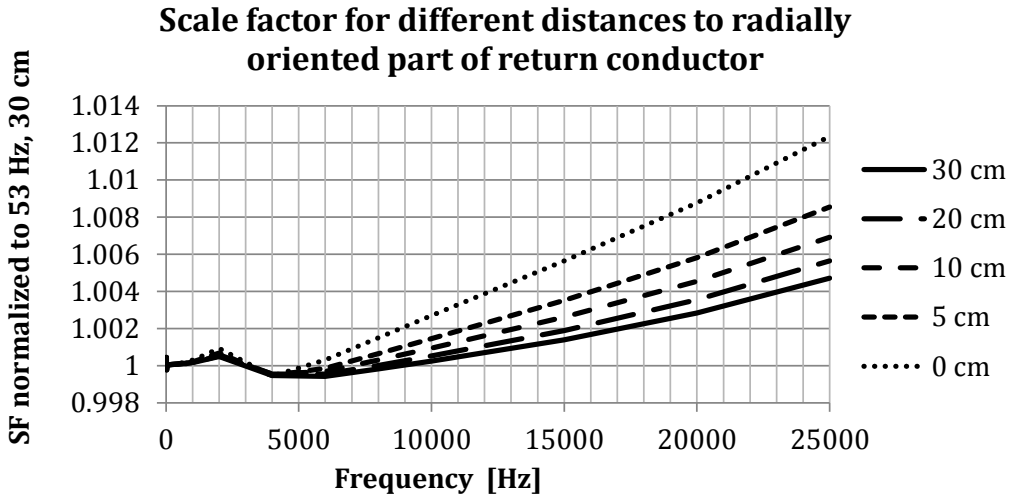

Figure 35: Normalized scale factor as a function of frequency for different distances to the radially oriented part of the primary current conductor.

With decreasing distance, SF increases which is equivalent to decreasing secondary current and output voltage. This is equivalent to a lower ampere-turns sensed by the secondary winding of the zero-flux sensor. Thereby a lower value of the primary current than the actually applied primary current is measured. The investigated parameter affects the detected magnetic field by introducing field components in a plane perpendicular to the primary current magnetic field. Further, the electro-magnetic environment of the cable connection point is affected. The exact physics behind the observed

SF behaviour has not been investigated. This is however not central to this thesis and is not further discussed.

In Figure 36, the normalized SF as a function of the distance to the radially oriented part is shown.

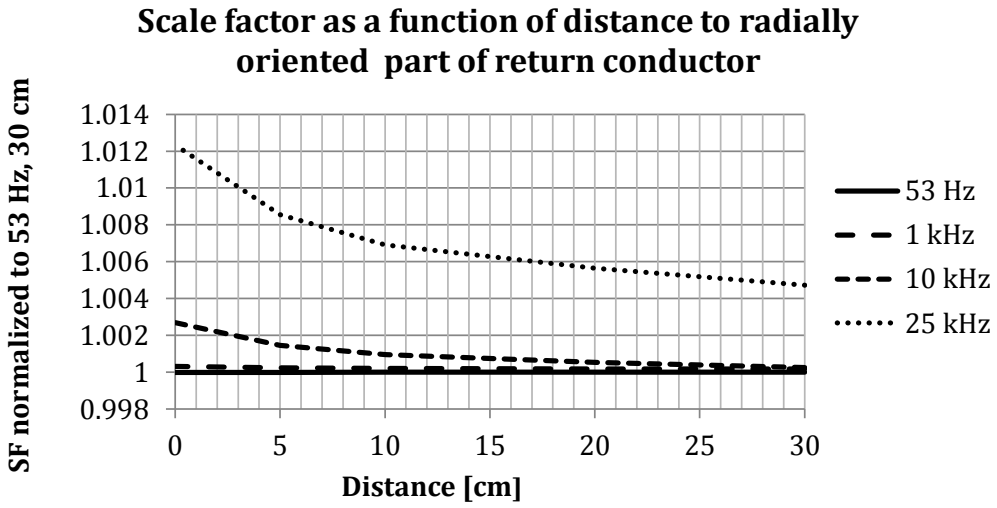

Figure 36: Normalized SF as a function of distance to the radially oriented part of the primary current conductor for some chosen frequencies.

For 53 Hz, the SF change is 0.0018 %, for 1 kHz 0.016 % and for 25 kHz 0.79 % for a distance of 0 cm as compared to the reference distance of 30 cm. These numbers are roughly half of the SF changes caused by de-centring in the previous section. In Figure 36, the SF is normalized to the SF value for 30 cm distance and 53 Hz. However, as can most distinctly be seen for the 25 kHz case, the effect on SF is most prominent when the distance becomes smaller than 10 cm, which is the minimum distance recommended by the manufacturer.

One possible way to avoid measurement errors related to distance to the radially oriented part of the return conductor is to perform measurements at some different distances with all other factors kept constant, and thereby find a distance where the influence from the radially oriented part of the return conductor is sufficiently small for the accuracy needed.

The practical implications are:

(1) the distance from the core to the radially oriented part of the return conductor is an important parameter to achieve correct measurements, and

(2) apart from the de-centring case, a very precise geometrical fitting of the sensor is not sufficient to avoid measurement errors. Measurements have to be performed to determine the sufficient distance in each specific case.

The effects become more pronounced the higher the measurement frequency.

5.3 Distance to return conductor

The magnetic field from the parallel part of the return conductor (Figure 28) affects the field sensed by the core by introducing a magnetic field in the same plane as that from the primary conductor. In Figure 37 the normalized SF is plotted as a function of frequency for some distances to the return conductor.

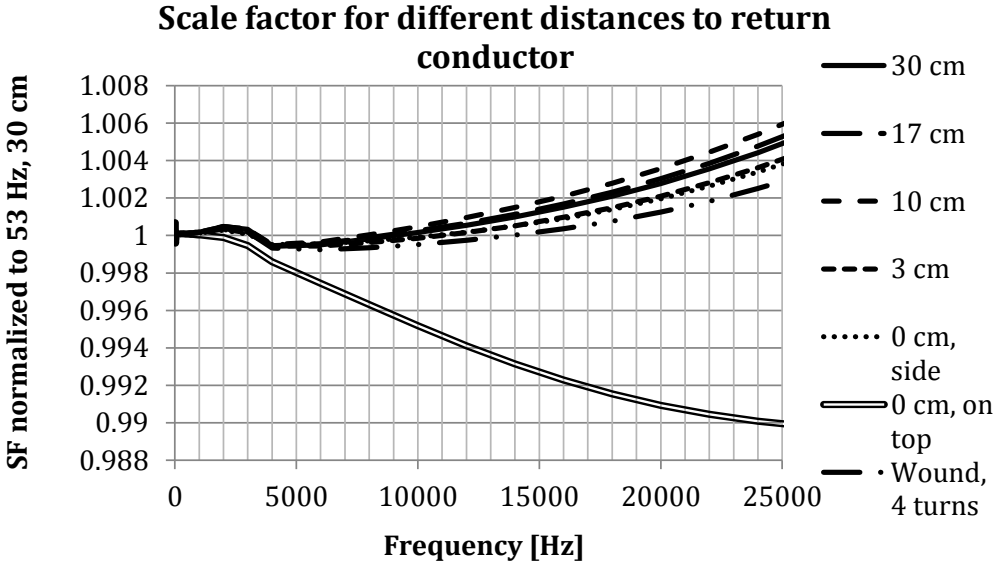

Figure 37: Normalized SF as a function of frequency for some distances to the return conductor.

Using the 30 cm distance measurement at 53 Hz as reference, we see that the SF increases for the 17 cm and 10 cm distances, but then decreases for 3 cm and 0 cm. The influence from the magnetic environment on the measuring cable connection point is again confirmed by the bottom double line in Figure 37, representing the case where the primary current return conductor was put directly on top of the measuring cable connection point.

A measurement representing another common practice, where the primary conductor is wound tightly around the core, is also shown in this Figure 37 and represented by the dashed-dotted line. Here, the primary conductor was wound four times around the sensor with one turn directly on top of the cable connection point. It is interesting to note that the winding case has the flattest high-frequency response. The winding procedure lowers the necessary supplied current – with four turns only one fourth of the current must be supplied from the current source to achieve the desired equivalent primary current in the zero-flux system. Since this practice lowers the current in each turn, it also lowers the local magnetic field caused by the return conductor with a factor equal to the number of turns, and the influence on the SF will be smaller as compared to the above mentioned worst case where the single return conductor was put on top of the cable connection point. In the four-turns case the primary cable will go diagonally across the core, which may account for the effect of being on top of the cable connection point is much smaller than ¼ of the single turn case.

Below 1 kHz, the SF difference is within 0.02 % for all configurations, and well within 0.01 % for all configurations except the on-top one, where the return conductor was placed directly on the cable connection point. At 110 Hz, the on-top configuration starts a rapid decline, but below 110 Hz, the SF stays within 0.005 % for all configurations.

In Figure 38, SF dependence on distance to the return conductor can be more clearly seen. SF as a function of distance is shown for some selected frequencies.

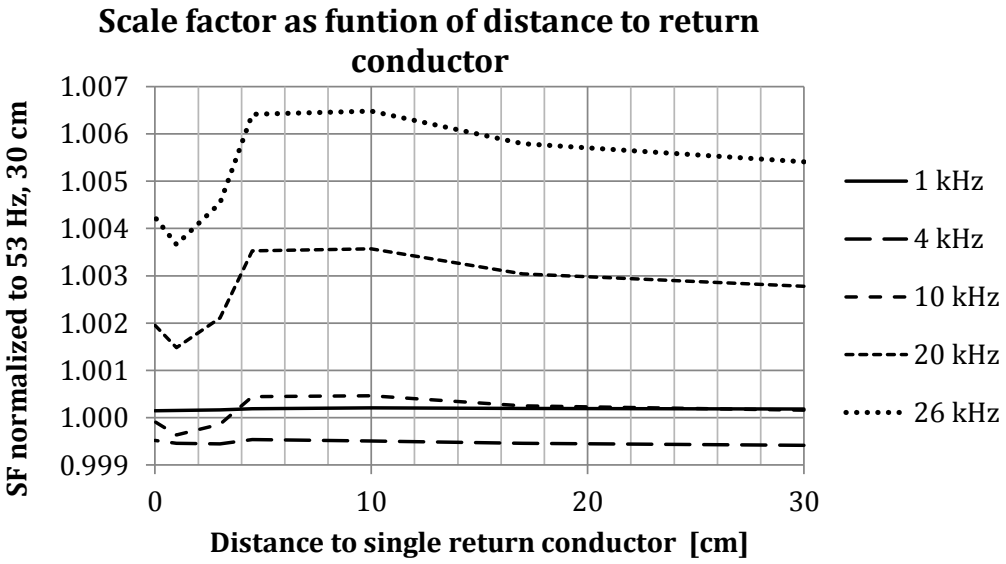

Figure 38: Normalized SF as a function of distance to the return conductor for some chosen frequencies.

For frequencies below 4 kHz, the SF is very little influenced by the distance to the return conductor – the curves are flat (here represented by the 1 kHz curve), and above 10 cm, the SF change is below 10^{-4}. Above 4 kHz, a more dramatic effect on the SF can be seen. The characteristic is not flat even at a distance of 30 cm, implying that there is an influence from the return conductor's magnetic field even at this distance. Further, for decreasing distances to the return conductor, the SF first increases (corresponding to decreasing indicated primary current) then decreases to a minimum at a distance of 1 cm (i. e. increasing indicated primary current), and then finally increases again, as the return conductor is in contact with the core outer circumference.

A possible interpretation is that this latter effect is caused by the interference with the cable connection point – the same effect as in the de-centring part, Figure 30. Referring to section 2.3 and 5.2, and the discussed transition between active compensation and passive AC mode, the increased sensitivity to the distance to the return conductor we can see above 4 kHz coincides with this change of operating modes.

The practical implications are:

(1) the distance from the core to the return conductor has a small influence on the SF below 4 kHz, and especially so when the distance is greater than 10 cm.

(2) above 4 kHz, the distance from the core to the return conductor is a rather important parameter to achieve correct measurements, and it should be characterized for each specific core.

5.4 Tilt

Tilt of the primary conductor relative to the sensor introduces a magnetic field component in a plane perpendicular to what the sensor is intended to pick up. The core experiences a non-symmetric magnetic field distribution as the distance between the core and the primary conductor is not the same for the whole sensor. Tilting locally enhances the field component in the direction that the core is designed to pick up on both sides of the core where the primary conductor is closer to the conductor. On the other hand, tilting also turns the field, creating the aforementioned field component that is perpendicular to the field that the sensor is designed to pick up, thereby lowering the total magnetic field that the sensor can pick up. These two geometrical effects hence oppose each other, and the total SF effect of tilting is expected to be small.

The maximum tilt angle α is limited due to geometrical constraints, thus the influence from tilt should be small. In this investigation, the maximum possible α is circa 30°. In Figure 39, the normalized SF is shown as a function of frequency for no tilt, maximum tilt ($+\alpha$ and $-\alpha$) around the y-axis as defined in Figure 27b and for maximum tilt around the x-axis, towards the cable connection point.

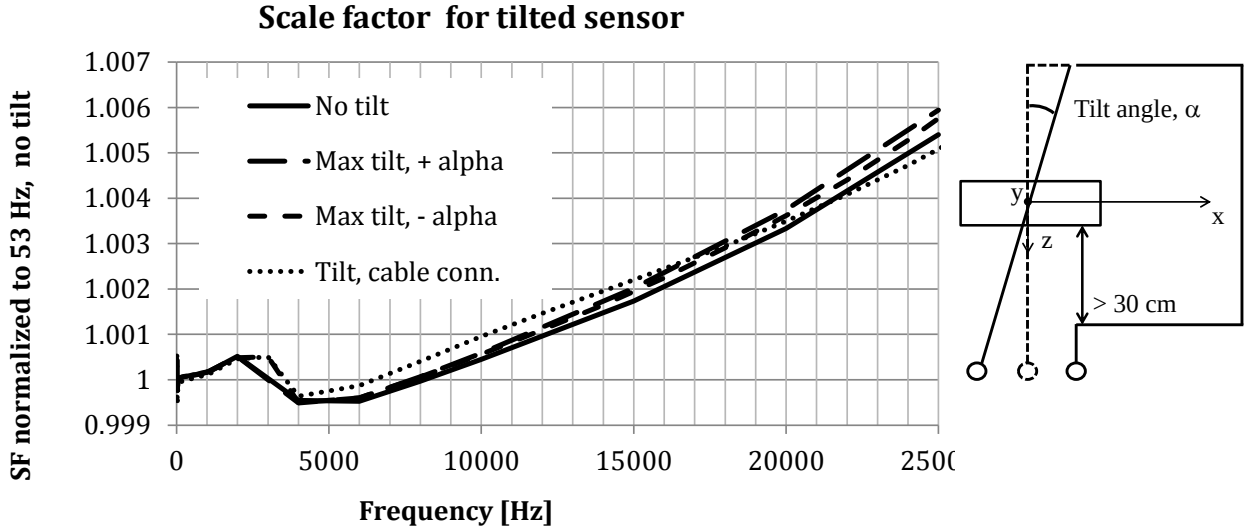

Figure 39: Left: Normalized SF as a function of frequency for different tilt angles. **Right:** Definition of tilt angle, Figure 27 repeated.

Figure 39 confirms that the influence from tilt is comparably small. The differences between $+\alpha$ and $-\alpha$ can even be due to a not perfect measuring arrangement, where the amplitude of $+\alpha$ and $-\alpha$ are not exactly the same. Tilt in the x-z-plane (i.e. not affecting the distance from the primary conductor to the cable connection point) gives slightly larger frequency dependence for frequencies above circa 2 kHz. Tilt in the y-z-plane (i.e. tilt that does affect the distance to the cable connection point) causes a somewhat flatter frequency response for the whole frequency range, but to the price of a larger SF changes already from 2 kHz and upwards.

Tilt not affecting the distance to the cable connection point causes small measurement errors, within $25 \cdot 10^{-6}$ below 1 kHz. Tilt that affects the distance between the primary conductor and the cable connection point causes a slightly different shape of the curve, and measurement errors up to $300 \cdot 10^{-6}$ below 1 kHz. Below 25 kHz, the maximum error for tilt is within 0.16 %.

The frequency dependence in Figure 39 is the normal frequency dependence of the sensor itself, and is not an effect of investigated parameter.

The practical implications are:

(1) tilt of the core relative to the primary conductor has a small influence on the measured SF compared to the influences from other geometrical asymmetries.

(2) it is easy to avoid error components due to tilt of the core by careful geometrical fitting of the sensor.

5.5 Rotation

The core is not perfectly circular symmetrical, because of the cable connection point disturbing the symmetry of the core and the windings. Hence rotation of the sensor around its axis of symmetry can cause errors. There are two possible influences, (1) the effect of the magnetic field on the measurement and zero-flux control cable itself, and (2) the effect of the magnetic field on the point where the cable is physically attached to the sensor. The effect on the measurement and zero-flux control cable itself is due to the enclosed time-varying magnetic field of the cable loop. Depending on how the twisting is done, there is also a larger or smaller effect from the electric field. Effects from the magnetic environment on the zero-flux control cable were seen also in section 5.1.

In this investigation, rotation angles in the span $\gamma = 0 - 540°$ are considered. The angle $\gamma = 0°$ corresponds to the case where the cable connection point is outside the primary current loop, see Figure 28, and $\gamma = 180°$ corresponds to the case where the sensor has been turned half a turn around its axis of symmetry. The angle $\gamma = 360°$ corresponds to a position of the cable connection point equivalent to $\gamma = 0°$, but now the measurement and zero-flux control cable is wound one turn around the sensor. $\gamma = 540°$ positions the cable connection point at the same place as the $\gamma = 180°$ case, but now the measurement and zero-flux control cable is wound 1.5 turns around the sensor. No experimentalists in their right mind would apply this practice in an actual measurement setup, but it serves to show an effect which cannot easily be shown otherwise. In Figure 40, the normalized SF is shown as a function of frequency for some different rotation angles. The SF is normalized to the measured SF at 53 Hz, $\gamma = 0°$.

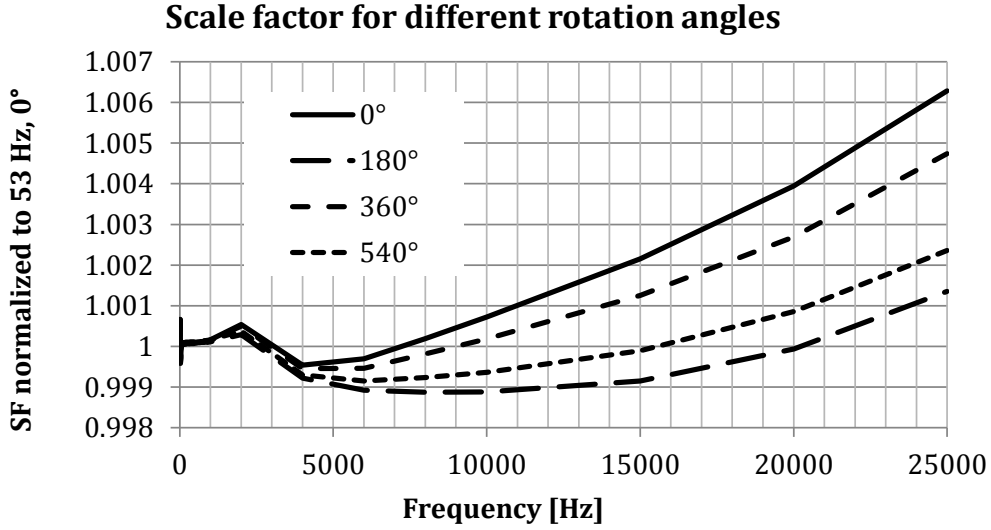

Figure 40: Normalized SF for different positions of the cable connection point.

Placing the cable connection point at $\gamma = 0°$ or at $\gamma = 180°$ cause an SF change of circa 0.5 % at 25 kHz. This change is caused by both the changed magnetic environment for the cable connection point and for the cable. For $\gamma = 0°$ and $\gamma = 360°$ (and $\gamma = 180°$ and $\gamma = 540°$) the magnetic environment for the cable connection point is the same, and the difference of circa 0.1 % at 25 kHz of these two curve combinations can be attributed to the changed environment for the cable. Hence the SF change caused by the changed magnetic environment on the cable connection point is just above 0.4 %

at 25 kHz.

The practical implications are:

(1) The position of the cable connection point relative to the magnetic fields in the measurement setup plays an important role to achieve correct measurements

(2) The positioning of the cable itself in the measurement setup plays an important role to achieve correct measurements. This effect is however very hard to isolate in the setup, and it must be addressed by separate considerations, such as choice of cable properties and choice of equipment.

(3) When preparing the measurement setup, care should be taken to keep both the cable connection point and the cable itself away from any fields. However, error due to rotation of the sensor cannot be avoided; instead measurements must be performed to find a reasonable measurement uncertainty component.

The effects become more pronounced the higher the measurement frequency.

5.6 Scale factor effects of primary current loop geometry

In the following section the maximum errors due to geometry of the primary current loop and the mounting of the sensor are summarized, followed by an uncertainty contribution estimation.

5.6.1 Maximum measurement errors

In Table VI the maximum SF changes due to the previously studied effects from the geometry of the primary current loop are summarized for some chosen frequencies. The exact numbers are specific to the zero-flux system utilized, but the procedure followed is however generally applicable. The table hence serves as examples of the significance of the investigated factors. Both a maximum observed SF change and a worst-case-excluded SF change are reported. The worst cases involve bringing the current conductor close to the cable connection point, which is only one of the phenomena we want to bring attention to. It would obscure the other phenomena – the influences from for example de-centring and varying distance to the radially oriented return conductor – and hence a result with this worst case excluded is also given.

For 53 Hz, the difference between the maximum observed SF change and the worst-case-excluded SF change is firstly very small and secondly, the worst case is not always the same as for the higher frequencies. Hence, only the maximum observed SF change is given in the table.

Table VI. Maximum variation in measured scale factor and variation in scale factor when the worst case is excluded.

	53 Hz	1 kHz		10 kHz		25 kHz		
	Max [%]	Worst case excluded [%]	Max [%]	Worst case excluded [%]	Max [%]	Worst case excluded [%]	Max [%]	Worst case defined by:
De-centring	0.0039	0.0084	0.0096	0.22	0.44	0.77	1.5	Close to cable conn.
Distance to radially oriented part of return conductor	0.0014	---	0.014	---	0.24	---	0.76	---
Distance to return conductor	0.0041	0.020	0.018	0.095	0.53	0.32	1.7	On top of cable conn
Tilt	0.0006	---	0.0062	---	0.011	---	0.084	---
Rotation	0.0026	---	0.0055	---	0.19	---	0.49	---

Many observations can be made from the table, and below some chosen ones are accounted for:

- The factors causing the largest changes at 25 kHz are de-centring (1.5 %) and too small distance to the return conductor (1.7 %). These are for the worst case scenarios, where the effects on the internal cable connection point are maximized. With this single worst case omitted, de-centring and distance to the radially oriented return conductor cause similarly large SF changes (circa 0.8 %). Tilt causes the smallest effect.

- At 53 Hz, it is interesting to note that rotation of the sensor has such a large influence, more than half as large influence as de-centring and distance to the return conductor. When positioning equipment such as generators and cables it is hence important to create a "corridor" for the measurement and zero-flux control cable, as free as possible from stray fields. It is also interesting to note that the distance to the radially oriented part of the return conductor plays a relatively small role compared to the distance to the parallelly oriented part (return conductor in the table). Given limited space, it is consequently more important to form a primary current loop with large distance to the parallel part of the return conductor, while the distance to the radially oriented part is not as important.

- The SF error increases with frequency for all investigated factors, but most for the distance to radially oriented part of return conductor (with a factor of over 500 times between 53 Hz and 25 kHz) and less for tilt and rotation (circa 150 times).

- The physical phenomena due to geometrical configurations can be classified as follows:
  - uneven distribution of the magnetic field from the primary conductor in the magnetic core (de-centring, tilt),
  - pick-up of magnetic fields with another origin than the primary conductor (distance to different parts of the return conductor),
  - effects on the cable (rotation) and the magnetic conditions in the cable connection point (all of the investigated factors).

5.6.2 Uncertainty contribution estimates

In this context, a comparison between the maximum SF changes shown in Table VI and the measurement uncertainty in RISE's commercially utilized measurement methods is near at hand. This comparison serves as an example of how this work can be taken as a template for performing studies on equipment and measurement setups to estimate the associated measurement uncertainty. However, two differences between these table values and the measurement uncertainty in accredited measurement methods are important to note. First, the errors given in the table represent the worst measurement conditions that are possible to create when it comes to geometry of the primary current loop. In contrast, creating a measurement uncertainty budget involves finding the maximum estimates for the uncertainties, given a reasonable care when mounting the equipment. Secondly, the table values represent only errors due to geometrical imperfections in mounting. In a measurement uncertainty budget, all possible impacting factors, such as temperature, variation of the measurand and instrument uncertainties are considered.

In RISE's methods for measurements utilizing the magnetic zero-flux technique, the best achievable measurement uncertainties for SF, are

- 50 ppm (=0.0050 %) at 50 Hz
- 200 ppm (=0.0200%) at 1 kHz
- 440 ppm (=0.0440 %) at 2.5 kHz (not included in Table VI above)

The first thing to note when comparing these measurement uncertainties with Table VI is that a careless handling of for example centring or distance to the return conductor may cause one of these single factors to become a dominating contribution to the measurement uncertainty.

Altogether, the results of Chapter 5 show that the influence of de-centring, distance to different parts of the return conductor, tilt and rotation cannot always be neglected. It is however possible to set up an uncertainty budget that takes into account reasonable and practically achievable requirements for these parameters, which can be used to develop a corresponding uncertainty contribution. Such requirements and the resulting input to uncertainty calculations will now be discussed.

For the reader unfamiliar with internationally established and accepted uncertainty calculations according to GUM (Evaluation of measurement data — Guide to the expression of uncertainty in measurement), [3] is recommended. In the following, the slightly simplified standard procedure according to EA 4/02 (Evaluation of the Uncertainty of Measurement In Calibration) for calculation of measurement uncertainty is used [48].

The investigated geometrical factors are treated as uncorrelated. Further, this work involves no corrections, i.e. the recalculation of a measured value due to a change in a parameter. It is worth to note that when no ideal case exists, we can only establish that the measured result varies between certain values and utilize this for an uncertainty estimate. When an ideal case on the other hand exists – like for example the de-centring case – corrective factors could in principle be obtained but are in this case omitted.

When estimating an uncertainty contribution, some considerations must be made: Firstly, as already mentioned above, a reasonable, practically achievable, requirement on the precision in mounting should be determined – or if the uncertainty contribution is still unduly large, the reverse procedure must be adopted; a maximum allowed requirement be determined, and then the practical tools for achieving this requirement must be found. Secondly, given the set of available data, the corresponding probability distribution should be applied. A randomly distributed variable is expected to show a Gaussian distribution. Some other distributions are the rectangular, where the probability for the measured value to be equal to the true value is the same over the interval; the triangular where the probability for the measured value to be equal to the true value is highest in the centre of the interval and then declines linearly towards zero at the interval extremes. In this work the Gaussian and the rectangular probability distributions are utilized. Thirdly, the above mentioned requirements need to be translated into SF difference, or to put it in simple terms: “x cm de-centring corresponds to y change in scale factor”.

For an ideal case, such as de-centring or tilt, the maximum SF deviation from the ideal case will be divided by the corresponding maximum distance (or angle in the tilt case) to get an estimate of SF sensitivity. This estimate is the sensitivity factor of EA-4/02. On the other hand, for the cases of the distances to the return conductor, the following simplified reasoning applies: for a distance change from x cm to y cm (here x = 30 cm and y = 10 cm were chosen), the SF change is ΔSF. As long as the parameter is within x to y cm, the resulting SF change is within ΔSF. A rectangular probability distribution is utilized.

In Table VII, the standard uncertainty contributions from the different geometrical imperfections as obtained from this work are calculated. The combined standard uncertainty is calculated as the root-summed-square (the square root of the sum of the contributions squared) of the standard uncertainties.

Note bene:

- For de-centring “SF change” is the change between ideal (centred position) and the position giving the largest SF deviation.
- For the distances to different parts of the return conductor, “SF change” is the variation between 10 cm and 30 cm distance from the core.
- For tilt “SF change” is the change between ideal (no tilt) and the position giving the largest SF deviation.
- For rotation, “SF change” is the change between 0 degrees and 180 degrees which give the largest SF change.
- The maximum SF deviations for de-centring are calculated as the SF difference between

centred position and the position giving the largest SF deviation for each frequency.

- The maximum SF deviations for the distances to the return conductor are calculated as the SF difference between the SF at a 30 cm distance and at a 10 cm distance at each frequency.
- The maximum SF deviations for tilt are calculated as the SF difference between a tilt of 0° and the position giving the largest SF deviation for each frequency.
- The maximum SF deviations for rotation are calculated as the SF difference between a rotation of 0° and the rotation giving the largest SF deviation for each frequency.
- The standard uncertainty, denoted by u, contribution for de-centring is calculated as:
  $$u = \frac{maximum\ SF\ deviation}{inner\ radius\ of\ sensor} \cdot suggested\ requirement \cdot probability\ distribution$$

- The standard uncertainty contributions for the distances to the return conductor and for rotation are calculated as:
  $$u = maximum\ SF\ deviation\ \cdot probability\ distribution$$

- The standard uncertainty contribution for tilt is calculated as:
  $$u = \frac{maximum\ SF\ deviation}{maximum\ tilt} \cdot suggested\ requirement \cdot probability\ distribution$$

The expanded measurement uncertainty is calculated as twice the combined standard uncertainty.

Table VII. Calculated uncertainty contributions from the investigated geometrical factors at 50 Hz and 1 kHz.

			50 Hz		1 kHz	
	Probability distribution	Suggested requirement	Max SF dev. [%]	**Standard uncertainty, u [%]**	Max SF dev. [%]	**Standard uncertainty, u [%]**
De-centring [cm] (diam=3.5 cm)	Gaussian, ½	±0.5 cm	0.0014	**0.0002**	0.0060	**0.0009**
Distance to radially oriented part of return conductor [cm]	Rectangular, $1/\sqrt{12}$	10 cm < "distance" < 30 cm	0.0004	**0.0002**	0.0020	**0.0006**
Distance to return conductor [cm]	Rectangular, $1/\sqrt{12}$	10 cm < "distance" < 30 cm	0.0009	**0.0003**	0.0012	**0.0004**
Tilt [degrees] (max tilt = 30°)	Gaussian, ½	±5 °	0.0093	**0.0008**	0.0057	**0.0005**
Rotation	Rectangular, $1/\sqrt{12}$	0°< "angle" < 180°	0.0031	**0.0009**	0.0056	**0.0016**
Expanded measurement uncertainty from contributions above:				**0.0024 0.0024**		**0.0040 0.0040**

The expanded measurement uncertainties in Table VII can now be compared with RISE's best achievable measurement uncertainties for SF. At 53 Hz we arrive at 24 ppm (0.0024 %) in Table VII, which is within RISE´s best achievable measurement uncertainties of 50 ppm (0.0050 %). At 1 kHz we arrive at 40 ppm (0.0040 %), well within RISE´s best achievable measurement uncertainties of 200 ppm or 0.0200 %. At 1 kHz, it is worth to note that the dominating contribution to the measurement uncertainty is the rotation of the sensor.

At 10 and 25 kHz there are no tabulated best achievable measurement uncertainties to compare with. However, an uncertainty contribution due to geometrical factors can still be computed, which is done in Table VIII. The same calculations and reasoning as in Table VII are used.

Table VIII. Calculated uncertainty contributions from the investigated geometrical factors at 10 and 25 kHz.

			10 kHz		25 kHz	
	Probability distribution	Suggested requirement	Max SF dev. [%]	**Standard uncertainty, u [%]**	Max SF dev. [%]	**Standard uncertainty, u [%]**
De-centring [cm] (diam=3.5 cm)	Gaussian ½	±0.5 cm	0.27	**376 0.038**	0.92	**0.13**
Distance to radially oriented part of return conductor [cm]	Rectangular $1/\sqrt{12}$	10 cm < "distance" < 30 cm	0.070	**203 0.020**	0.22	**0.064**
Distance to return conductor [cm]	Rectangular $1/\sqrt{12}$	10 cm < "distance" < 30 cm	0.030	**88 0.0090**	0.069	**0.020**
Tilt [degrees] (max tilt = 30°)	Gaussian ½	±5 °	0.050	**42 0.0040**	0.050	**0.013**
Rotation	Rectangular $1/\sqrt{12}$	0°< "angle" < 180°	0.19	**531 0.053**	0.50	**0.15**
Expanded measurement uncertainty from contributions above:				**0.14**		**41 0.41**

From Table VIII, we can see that the uncertainty increases rapidly with frequency. The 0.0040% at 1 kHz has increased more than 100 times, to over 0.4% for 25 kHz for the geometrical factors. Also taking the frequency dependence into account, which for rotation is almost 0.7% and for distance to the return conductor and tilt is near 0.6%, the conclusion is that if one wanted to make a CMC-statement, the uncertainty would probably end up somewhere between 1 and 2%. Also, considering the magnitude of the SF deviation to the 50 Hz case, we cannot characterise the total uncertainty at high frequencies based on the results available in this study.

It is also worth to note that rotation of the sensor is the, or one of the dominating uncertainty contributions for all frequencies, and even more so the higher the frequency.

5.7 Phase angle error effects of primary current loop geometry

For completeness, this section is dedicated to some phase angle error results. To achieve input to an uncertainty budget for the phase angle error, the same type of detailed analysis would need to be done as for the scale factor. Since the focus of this thesis is to pinpoint vital issues for optimal utilization of zero-flux technique rather than a complete uncertainty analysis, the analysis is however limited to some selected matters. Since de-centring was one of the investigated factors giving rise to the largest effects for scale factor, we will now look into some results for phase angle error.

Figure 41 shows the phase angle error as a function of frequency for different de-centering positions of the primary current conductor. Over the entire frequency range, a linear frequency dependence can be seen, where position 4 differs most from the linear curve. This is in agreement with the results of Figure 30, where the primary conductor position causing the largest effect on the cable connection point (position 4) also deviates most from the results of the centered position. However, it is position 6 and not the centered case that maintains the most linear behavior for increasing frequency. So far, the centered position has been considered the ideal case, since it gives the most symmetrical distribution of the magnetic field in the magnetic core. However, deeming from the results of Figure 41, the minimized interference with the cable connection point of position 6 gives the most linear frequency dependence, hinting that in the high frequency region, the magnetic environment of the cable connection point is more important than a symmetrical distribution of the magnetic field.

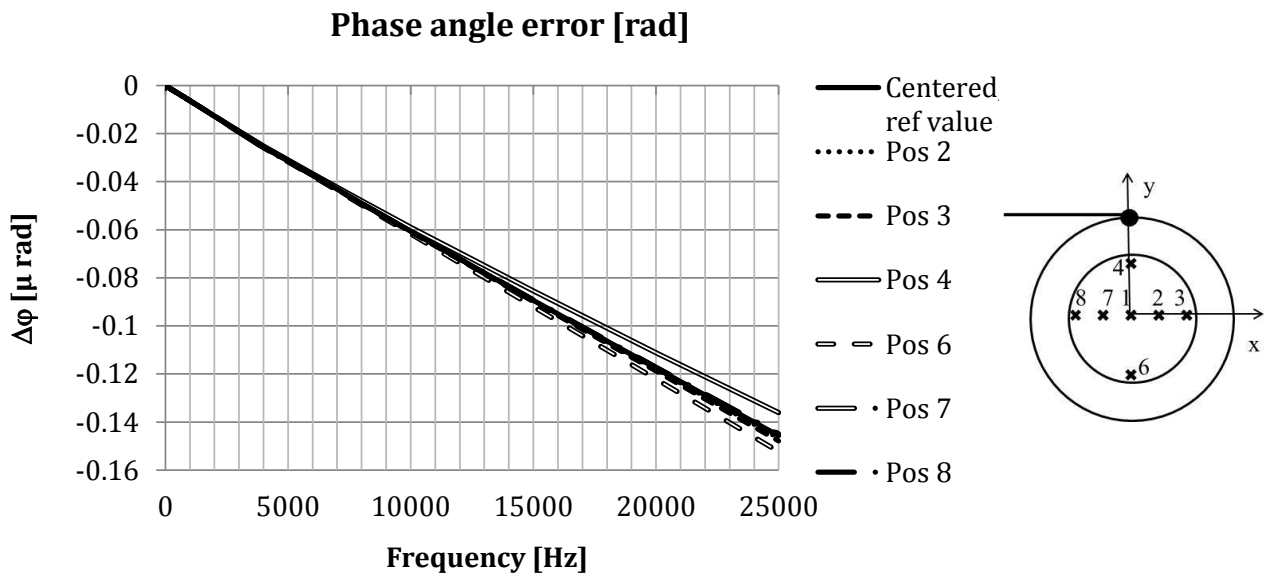

Figure 41: Phase angle error as a function of frequency.

The linearity seen in Figure 41 corresponds to a constant time delay, more clearly seen in Figure 42 and Figure 43, where the phase angle error divided by frequency ($\Delta\varphi/f$) is shown.

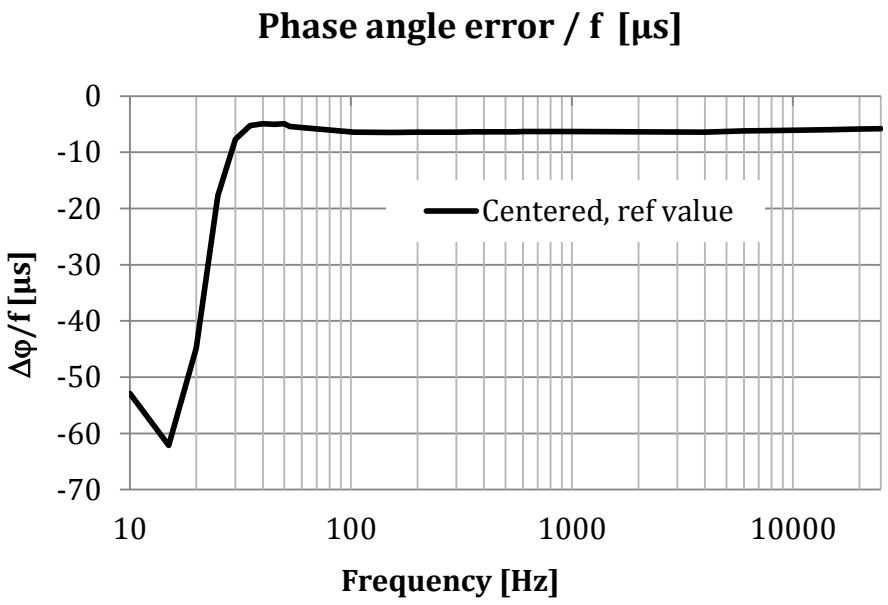

Figure 42: Phase angle error divided by frequency, as a function of frequency for 10 Hz to 25 kHz.

In Figure 42, only the curve of the centered position is shown, since no difference between the curves can be seen at this scale. Just like for the example in Figure 15 and Figure 20 the dip around 20 Hz can be seen, again it is important to note that the numerical value of this minimum is unique for the individual measuring system investigated, and in part depends of the tuning of the system. We can also see that for the higher frequencies, the measured phase angle error corresponds to a more or less constant time delay, independent of frequency.

In Figure 43, a y-axis zoom-in of $\Delta\varphi/f$ is shown. The transition region between the active compensation region and passive transformer region at a couple of kHz can again be seen. Moreover a similar behavior as for scale factor can be seen; de-centering along the y-axis causes a considerably larger effect than de-centering along the x-axis.

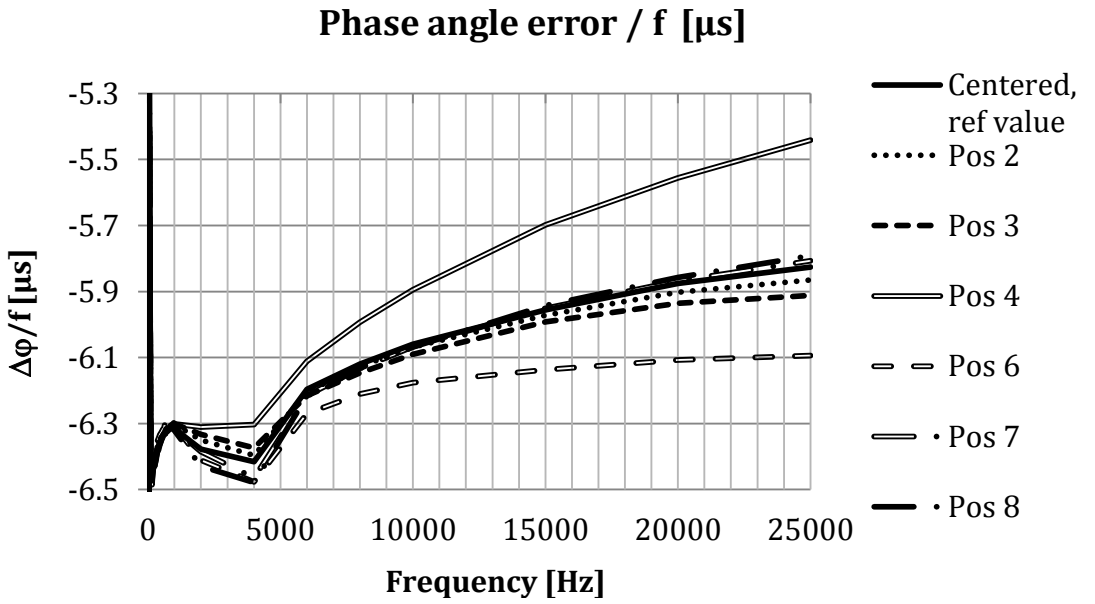

Figure 43: Y-axis zoom-in of the phase angle error divided by frequency, as a function of frequency.

The differences between the measured cases are comparably small, within 0.7 µs for 25 kHz, within 0.3 µs for 10 kHz, within 0.025 µs for 1 kHz and within 0.015 µs for 53 Hz. As an interesting comparison, the corresponding difference for 50 Hz is circa 1 µs.

In RISE's methods for measurements utilizing the magnetic zero-flux technique, best achievable measurement uncertainties for $\Delta\varphi/f$ are:

- 50 µrad at 53 Hz, corresponding to $\Delta\varphi/f$ = 1 µs
- 2000 µrad at 2 kHz, corresponding to $\Delta\varphi/f$ = 1 µs,
- For higher frequencies, the measurement uncertainty has to be achieved for each separate calibration.

The results above for phase angle error suggest that the performance of the zero-flux system will have similar properties as for SF. To achieve complete results also for phase angle error, the same analysis as for SF needs to be performed, but will not be done here.

5.8 Concluding remarks

The geometry of the primary current loop has been identified as an aspect of a non-contact current measuring setup that affects the measurement result. In this chapter, a procedure for the quantification and comparison of these errors is introduced and applied to a zero-flux current measuring system. Further, requirements for the geometrical aspects of the measuring setup are suggested and the resulting input parameters for an uncertainty analysis are calculated for scale factor.

Two separate physical phenomena can influence the performance of the current sensor as related to primary current loop geometry. Firstly, the magnetic field in the core can be influenced, either by asymmetry of the primary conductor or by stray fields. Secondly, stray fields can disturb the measuring electronics; an example of the latter is the strong influence on the measurement results from the magnetic field in the cable connection point.

At almost all evaluated frequencies, de-centring towards the cable connection point and too small distance between the core and the return conductor cause the largest variation in measured scale factor. The smallest variation in measured scale factor was for tilt, and at 25 kHz, tilt cannot be said to have any significant effect at all. The exception from above was 1 kHz, where the two largest variations came from too small distance to the radially oriented part of the return conductor and too small distance to the return conductor. The smallest contribution here came from rotation.

When examples of uncertainty contribution estimates due to scale factor variation are calculated, rotation is among the largest contributor for all examined frequencies. For 53 Hz, the uncertainty contribution from rotation is of the same order of magnitude as tilt, and the three other geometrical factors of minor importance. For 1 kHz and upwards, de-centring is the second largest contributor to measurement uncertainty. The expanded measurement uncertainties calculated in this work can serve as input parameters to an uncertainty budget, and are well in line with RISE's CMCs.

Around 1 kHz, the zero-flux measuring system leaves the active AC compensation mode and instead enters the passive AC mode. The increased sensitivity to de-centring, distances to different parts of the return conductor, tilt and rotation that can be seen for increasing frequencies coincides with this change of operating modes. The transition frequency may be different for different measuring systems.

An important result is that the magnetic field affecting the cable connection point is the single most important factor to control for frequencies in the passive AC mode. The other geometrical factors must however also be investigated to achieve a correct uncertainty analysis when evaluating an unknown zero-flux measuring system.

A conclusion from the results above is that it is possible to extend the frequency range where best achievable measurement uncertainty is established in RISE's methods. Only the linear region, i. e. the active AC compensation mode has so far been utilized, and the passive AC operating mode has been considered as "out of range" and has seldom been utilized. However, with proper care preparing the measurement setup, and due attention payed to the transition region, the results above hint that also the passive AC operating mode is predictable enough to be utilized as a measurement standard.

6 Conclusions

As stated in Chapter 1.2, this project aims at bringing up some vital issues for optimal utilization of zero-flux technique, within unspecified application field of AC current measurements. Focus has been to determine how sensitive the measurement results are to practical arrangements and limitations of the measurement setup.

Regarding phase angle error, the most vital issues identified are:

1. The phase angle error of a zero-flux current measuring system was found to be constant in time units in the frequency range of about 20 Hz to 2.5 kHz, and is hence possible to compensate for. The frequency normalized phase angle error $\Delta\varphi/f$, is proposed as a quantity characteristic to and useful for the evaluation of and comparison between different types of zero-flux systems. At about 5 Hz to 20 Hz, a transition between the DC mode and the active AC compensation mode was identified. At about 2.5 kHz, $\Delta\varphi/f$ seized to be constant, and the passive AC mode is entered.
2. The constant error, $\Delta\varphi/f$, is mainly introduced by the read-out buffers, while the active transformers in the active AC compensation mode have an error close to zero.
3. Adjustment of the AC loop gain can be utilized to extend the active AC compensation mode. The upper frequency limit was pushed from circa 1 kHz, corresponding to the 20^{th} harmonic, to circa 3 kHz, corresponding to the 60^{th} harmonic. However, the adjustment also broadened the transition region between the AC operation mode and the passive AC mode. The optimization will hence be a trade-off depending on application.
4. The introduction of an AC shunt resistor as read-out resistor reduced the phase angle error in the whole frequency span. It also reduced the high frequency SF error at 100 kHz quite dramatically, from 45 % for the built-in shunt to 3.5 %. The built-in shunt resistor works reasonably well below 9 kHz.

The four listed items above serve to identify the source of the measurement error in the zero-flux system's design and to minimize this error.

The method introduced and utilized in Chapter 5.1 - 5.5 can be utilized as a guide to the assessment on how different configurations of the measurement setup affect the measured results in different frequency ranges. Requirements for the geometrical aspects of the measuring setup are suggested and in Chapter 5.6, the resulting input parameters for an uncertainty analysis are calculated for scale factor.

Regarding the measurement error and the measurement uncertainty of a zero-flux system in presence of geometric asymmetry of the cabling and disturbances brought up by return, or nearby located, conductors, the most vital issues identified are:

1. At almost all evaluated frequencies, de-centring towards the cable connection point and too small distance between the core and the return conductor cause the largest variation in measured scale factor. The exception was 1 kHz, where the largest variations came from too small distances to the return conductor.
2. In the passive AC mode the effects of geometrical factors of the primary current loop become more pronounced than in the active AC compensation mode. The magnetic field affecting the cable connection point is the single most important factor to control for frequencies in the passive AC mode.
3. When examples of uncertainty contributions estimates due to scale factor variation are calculated, rotation is among the largest contributor for all examined frequencies. The expanded measurement uncertainties calculated in this work can serve as input parameters to an uncertainty budget, and are well in line with RISE's CMCs.

4. The results above hint that it is possible to extend the frequency range where best achievable measurement uncertainty is established in RISE's methods also into the passive AC operating mode, with the important implication that the frequency range for traceable measurements available to industry is improved.

Simultaneous measurement of sinusoidal signals of different amplitudes, frequencies and phase angle errors was identified as a significant aspect, but left outside the scope of this thesis.

Regarding the detection of transient and sub-synchronous events, much work remains, but an identified issue, vital for measurement applications concerning the railway grid utilizing $16^{2/3}$ Hz, is that one of the zero-flus systems had its maximum phase angle error at circa 17 Hz.

7 Future Work

AMONG the aspects of interest identified in 1.2, simultaneous measurements of sinusoidal signals of different amplitudes, frequencies and phase angles (iii), detection of sub-synchronous events (iiii), and non-steady state phenomena (v) have mainly been left out of the scope of this theses.

To further assess some of these aspects, this work can be continued by for example the following set of investigations:

(1.) How is the measurement error of the sensor affected by one, or ideally two, current conductor(s) close-by, carrying a current of the same amplitude, but 120 degrees out of phase? This experiment imitates the disturbance situation in a three-phase installation and can be performed utilizing the same equipment as in the thesis with one (or two) additional set(s) of current generating equipment.

(2.) Utilizing two phase-locked Fluke 5700, an arbitrary phase shift between the two currents in (1.) can be generated. The practical use of this investigation can be hard to motivate, but ideally, these measurements could help to develop a theoretical way to predict how the sensor properties depend on the phase shift of a near-by phase shifted current.

(3.) How is the measurement of high-frequency components affected if there is a large 50 Hz bulk current present in the sensor as well? By utilizing two current sources and two conductors, a 50 Hz bulk current can be applied through the sensor, together with a small kHz frequency current.

(4.) An investigation of how the measurement is affected by the number and placement of turns of the primary conductor through the sensor would give information on the measurement error due to winding. Winding of the primary conductor is a common practice to obtain higher current amplitude, and for the high accuracy measurements, the result will vary depending on how the winding is performed. In this context it would also be interesting to compare the current dependence with and without winding.

(5.) When addressing the measurement of sub-synchronous events, there is no reason to doubt that the DC-circuitry of the utilized zero-flux measuring systems can handle very low frequencies also in the sub-Hz range. However, a full characterization needs to be done, and the first step is to find the proper equipment, both for generation and reference measurement of the low frequencies. In this thesis characteristics have been obtained down to 5 Hz, which is the frequency limit of the utilized DSWM system. The dip in the phase angle characteristics around 17 Hz needs to be further investigated, which could be done utilizing the same equipment as in this thesis.

8 References

[1] S. v Friesen, *Om mått och män*, Bra Böcker, 1987.

[2] http://www.bipm.org/en/measurement-units/ Accessed March 18, 2017.

[3] "JCGM 100:2008 Evaluation of measurement data — Guide to the expression of uncertainty in measurement" http://www.bipm.org/utils/common/documents/jcgm/JCGM_100_2008_E.pdf; last accessed Nov. 18, 2016.

[4] A. Hobson, "The Zero-Flux Current Transformer": Power Apparatus and Systems, Part III. Trans. of the American Institute of Electrical Engineers, Vol. 72 , Issue: 2, Jan. 1953.

[5] P. N. Miljanic, "Current transformer with internal error compensation" US patent US 3534247 A, Oct 13 1970.

[6] A. Wright, *Current transformer*, Capman and Hall Ltd, 1968.

[7] IEEE Working Group on Power System Harmonics, "Power system harmonics: An overview," IEEE Trans. Power App. Syst., vol. PAS-102, pp. 2455–2460, Aug. 1983.

[8] G. K. Singh, "Power system harmonics research: a survey", European Trans. on Electrical Power, Vol. 19, Issue 2, pp. 151–172, Mar. 2009.

[9] T. M. Gruzs, "A survey of neutral currents in three-phase computer power systems", IEEE Trans. on Industry Applications, Vol. 26, Issue 4, pp. 719 - 725, Jul/Aug 1990.

[10] D. Chapman, "Application note harmonics: Causes and effects", European Copper Institute, ECI Publ. No Cu0119 Available from www.leonardo-energy.org /node/1283 Nov. 2011.

[11] R. D. Henderson, P. J. Rose, "Harmonics: The Effects on Power Quality and Transformers", IEEE Trans. on industry appl., Vol. 30, No. 3, May 1994.

[12] IEEE Working Committee Rep.: M. R. Iravani, B. L. Agrawal, D. H. Baker, C. E. J. Bowler, R. G. Farmer, R. A. Hedin, E. H. V. Larsen, J. F. Tang, "Fourth supplement to a bibliography for the study of subsynchronous resonance between rotating machines and power systems", IEEE Trans. on Power Systems, Vol. 12, No. 3, Aug. 1997.

[13] P. M. Anderson, B. L. Agrawal and J. E. Van Ness, *Subsynchronous resonance in power systems*, John Wiley & Sons, 1999.

[14] R. K. Varma, S. Auddy and Y. Semsedini, "Mitigation of Subsynchronous Resonance in a Series-Compensated Wind Farm Using FACTS Controllers", IEEE Trans. on power delivery, Vol. 23, No. 3, Jul. 2008.

[15] C. v Schultz, "Åskan slår ut nya led-lampor", in Ny Teknik 2015, " http://www.nyteknik.se/nyheter/askan-slar-ut-nya-led-lampor-6394000" last accessed Jan. 11, 2017.

[16] K. H. Weck, et al, "European intercomparison of high-current measuring systems of high-power laboratories to establish traceability", in Proc. Measurement and calibration in high voltage testing, pp. 1/1.1-3, 1998.

[17] E. So, R. Arseneau, D. Bennett, T. L. Nelson, B. C. Waltrip, "NRC-NIST intercomparison of calibration systems for current transducers with a voltage output at power frequencies", IEEE Trans. on Instrumentation and Measurement, vol. 52, no. 2, pp. 424-8, Apr., 2003.

[18] M. Klonz, H. Laiz, T. Spiegel, P. Bittel, "AC-DC current transfer step-up and step-down calibration and uncertainty calculation", IEEE Trans. on Instrumentation and Measurement, vol. 51, no. 5, pp. 1027-34, Oct., 2002.

[19] J.P.M. de Vreede, "CCE intercomparison of AC-DC transfer standards", IEEE Trans. on Instrumentation and Measurement, vol. 42, no. 2, pp. 99-108, Apr., 1993.

[20] K. Bohnert, P. Gabus, H. Brändle, P. Guggenbach, “Fiber-optic dc current sensor for the electro-winning industry”, in Proc. of the SPIE - The Int. Society for Optical Engineering, vol. 5855, pp. 210-13, 2005.
[21] J. L. Stokes, R. R. Bartsch, J. C. Cochrane, R. E. Chrien, P. J. Forman, L. D. Looney, L. J. Tabaka, L. R. Veeser, B. R. Marshall, W. B. Broste, B. J. Warthen, “Precision current measurements on Pegasus II using Faraday rotation”, in Digest of Tech. Papers. Tenth IEEE Int. Pulsed Power Conf. (Cat. No. 95CH35833), p 378-83 vol.1, 1995.
[22] W. J. M. Moore and P. N. Miljanic, *Current Comparator*, 1st ed., Peter Peregrinus, 1988, ISBN-10: 0863411126.
[23] H. C. Appelo, M. Groenenboom, J. Lisser, “The zero flux dc current transformer a high precision bipolar wide-band measuring device”, IEEE Trans. on Nuclear Science, vol. NS-24, no. 3, 1977.
[24] K. B. Unser, “The parametric current transformer, a beam current monitor developed for LEP”, AIP Conference Proceedings 252, 266, 1992; doi: 10.1063/1.42124.
[25] J. Bergoz, “Current monitors for particle beams”, Nuclear Physics A525, 595c-600c, 1991.
[26] G. Fernqvist, H.-E. Jörgensen, A. Saab, “Design and verification of a 24 kA calibration head for a DCCT test facility”, IEEE Trans. on Instr. and Meas., vol. 48, no. 2, pp. 346-50, Apr. 1999.
[27] Y. Suzuki, A. Hirabayashi, K. Yamasawa, “Analysis of a zero-flux type current sensor”, IEEE Trans. on Magnetics, vol. 29, no. 6, pp. 3183-5-71, Nov., 1993.
[28] M. J. Garcia, A. Turo, “Improved zero-flux type large bandwidth current sensor,” Conf. Proc. IEEE Instr. and Meas. Technology Conf., Jun., 1996.
[29] M. H. Samimi, A. Mahari, M. A. Farahnakian, H. Mohseni, “The Rogowski Coil Principles and Applications: A Review”, IEEE Sensors Journal, vol. 15, no. 2, pp. 651-8, Feb., 2015.
[30] J. D. Ramboz, “Machinable Rogowski coil, design and calibration”, in Proc. IMTC, Waltham, MA, USA, pp. 329-34, 1995.
[31] J. P. Barber, “The use of Rogowski coils in current measurements”, in Proc. 17th Int. Symp. on Electromagnetic Launch Technology (EML), p 1-4, 2014.
[32] Y. Chekurov, J. Hällström, "Influence of busbar geometry on AC current measurement using Rogowski coil", in Conf. on Precision Electromagnetic Measurements Digest, p 542-3, 2008, doi: 10.1109/CPEM.2008.4574893.
[33] D. E. Destefan, “Calibration and testing facility for resistance welding current monitors”, IEEE Trans. on Instrumentation and Measurement, vol. 45, no. 2, pp. 453-6, Apr., 1996.
[34] E.-P. Suomalainen, J. K. Hällström, “Onsite calibration of a current transformer using a Rogowski coil,” IEEE Trans. on Instr. and Meas., vol. 58, no. 4, pp. 1054-8, Apr. 2009.
[35] D. Istrate, I. Blanc, D. Fortune, “Study and development of a measurement set-up for high impulse currents”, in Proc. CPEM, Washington DC, USA, pp. 224-5, 2012.
[36] Data sheet for coils from PearsonElectronics: http://www.pearsonelectronics.com/products/wideband-current-monitors Accessed May 27, 2017.
[37] Application note AE-010 from Athena Energy: http://athenaenergycorp.com/wp-content/uploads/2016/03/Rogowski-Product-Performance-Comparison.pdf Accessed May 2, 2017.
[38] *STACC IT2867/SL/LHC Zero-flux^{TM} USER MANUAL*, Doc. No. Man IT2867, Rev. 02, Hitec Power Prot., Almelo, The Netherlands, 2004.

[39] *TOPACC USER MANUAL Zero Flux^{TM} measuring system*; Doc. No. TOPACC; Revision 2, October 2003.

[40] *STACC USER MANUAL Zero-flux^{TM} Current Transformer*, Rev. 4, Hitec Power Prot., Almelo, The Netherlands, 2009.

[41] S. Svensson, "Power Measurement Techniques for Non-Sinusoidal Conditions", PhD thesis, Department of Electric Power Engineering, Chalmers, Gothenburg, Sweden, 1999.

[42] S. Svensson, "A Measuring System for the Calibration of Power Analyzers" IEEE Transactions on Instrumentation and Measurement, Vol. 44, No. 2, pp. 316-17, Apr. 1995.

[43] T. Bergsten, V. Tarasso and K.-E. Rydler, "Precision measurement system for characterisation of phase displacement of voltage dividers up to 1 MHz," in Proc. CPEM, Daejeon, South Korea, pp. 259-60, 2010.

[44] K.-E. Rydler, T. Bergsten and V. Tarasso, "Determination of phase angle errors of current shunts for wideband power measurement", in Conf. on Precision Electromagnetic Measurements Digest, p 284-5, July 2012.

[45] M. Hammarqvist, A.-P. Elg, A. Bergman, J. Blennow and S. M. Gubanski, "Investigation of the Frequency Dependency of Phase Angle Error in a Zero-Flux Current Measuring System", pres. at ISH, Seoul, Korea, Aug., 2013.

[46] M. Hammarqvist, A.-P. Elg, A. Bergman, J. Wolbert, J. Blennow and S. M. Gubanski, "Improvement of Frequency Response for a Zero-Flux Current Measuring System", pres. at CPEM, Rio de Janeiro, Brazil, Aug., 2014.

[47] http://www.bipm.org/exalead_kcdb/exa_kcdb.jsp?_p=AppC&_q=power+ac, last accessed: May 27, 2017.

[48] EA-4/02 Expression of the Uncertainty of Measurement in Calibration, url: http://www.european-accreditation.org/publication/ea-4-02-m-rev01-september-2013, last accessed: Nov. 18, 2016.